JCB Journal of Cell Biology

TOOLS

Analysis of conditional colocalization relationships and hierarchies in three-color microscopy images

Jesus Vega-Lugo[1*], Bruno da Rocha-Azevedo[1*], Aparajita Dasgupta[1], and Khuloud Jaqaman[1,2]

Colocalization analysis of multicolor microscopy images is a cornerstone approach in cell biology. It provides information on the localization of molecules within subcellular compartments and allows the interrogation of known molecular interactions in their cellular context. However, almost all colocalization analyses are designed for two-color images, limiting the type of information that they reveal. Here, we describe an approach, termed "conditional colocalization analysis," for analyzing the colocalization relationships between three molecular entities in three-color microscopy images. Going beyond the question of whether colocalization is present or not, it addresses the question of whether the colocalization between two entities is influenced, positively or negatively, by their colocalization with a third entity. We benchmark the approach and showcase its application to investigate receptor-downstream adaptor colocalization relationships in the context of functionally relevant plasma membrane locations. The software for conditional colocalization analysis is available at https://github.com/kjaqaman/conditionalColoc.

Introduction

Multimolecular interactions are the basis of cellular functions. High-resolution and super-resolution fluorescence microscopy allow us to routinely image three or more molecular entities at the same time within a cell (Huang et al., 2009; Sahl et al., 2017; Valm et al., 2017). Such multicolor imaging may provide a wealth of information about the spatiotemporal regulation of multimolecular interactions in their cellular context. However, without computational and quantitative analysis, much of this information remains unextracted (Bolte and Cordelières, 2006; Lagache et al., 2015).

Colocalization analysis is a cornerstone technique in cell biology for the analysis of microscopy images. It provides information on the localization of molecules within various subcellular compartments, shedding light on their function (Bolte and Cordelières, 2006; Dunn et al., 2011). While colocalization analysis may lack the spatial resolution necessary for the *de novo* identification of molecular interactions, it does allow the interrogation of known molecular interactions in their cellular context. This capability complements biochemical and biophysical techniques, which are often employed to establish interactions, but taken out of their cellular context (Caetano et al., 2015; Helmuth et al., 2010; Lagache et al., 2018; Lagache et al., 2015).

Colocalization analysis generally falls into one of two categories: (i) pixel/voxel-based, such as the Pearson correlation coefficient (Aaron et al., 2018; Adler et al., 2008; Bolte and Cordelières, 2006); and (ii) object-based, where first objects are detected or segmented in the images and then the colocalization between objects is analyzed (Lagache et al., 2015; Mascalchi and Cordelieres, 2019). Depending on the nature of the objects and the biological question, object-based colocalization analysis can then employ intensity (Manders et al., 1993), area/volume overlap (Mascalchi and Cordelieres, 2019), or inter-object distances (usually between object centroids; Boutte et al., 2006; Helmuth et al., 2010; Lachmanovich et al., 2003; Lagache et al., 2018; Pastorek et al., 2016). For the latter, colocalization analysis can be thought of as a spatial point pattern analysis task (Diggle, 2014; Lagache et al., 2015). With the advent of single-molecule localization microscopy, which yields data in the form of point coordinates, there have been many developments in colocalization analysis through point pattern analysis (Andronov et al., 2016; Malkusch et al., 2012; Pageon et al., 2016; Williamson et al., 2020).

In spite of the many developments and flavors of colocalization analysis, the overwhelming majority is applicable to only two-color microscopy images, i.e., they investigate only pairs of molecular entities at a time. The few previous studies involving three-color colocalization were mainly focused on the question of whether the three imaged entities colocalize (Fletcher et al., 2010; Stauffer et al., 2018). This limits the type of information

[1]Department of Biophysics, UT Southwestern Medical Center, Dallas, TX; [2]Lyda Hill Department of Bioinformatics, UT Southwestern Medical Center, Dallas, TX.

*J. Vega-Lugo and B. da Rocha-Azevedo contributed equally to this paper. Correspondence to Khuloud Jaqaman: khuloud.jaqaman@utsouthwestern.edu.

that they may reveal, leading to the underutilization of multicolor microscopy images.

Here, we developed an approach for analyzing the colocalization relationships between three molecular entities, termed "conditional colocalization analysis." It is based on the spatial point pattern analysis of detected objects in microscopy images, applicable to images of both punctate and non-punctate objects. Going beyond the question of whether colocalization is present, it addresses the question of whether the colocalization between two molecular entities is influenced, positively or negatively, by their colocalization with a third entity. For molecules known to interact, the extracted colocalization relationships provide evidence for the cooperativity or competition between interactions, and for the enhancement or suppression of interactions at subcellular locations, domains, or compartments. We benchmarked and validated the method using combinations of molecules known to interact or not interact with each other. To then highlight the capabilities of conditional colocalization analysis, we applied it to investigate the colocalization relationships between a receptor and its downstream adaptor in the context of functionally relevant plasma membrane locations.

Results

Derivation of conditional colocalization measures

To derive measures that reflect the extent to which one molecular entity influences the colocalization between two other molecular entities, we took an object-based approach (Lagache et al., 2015; Mascalchi and Cordelieres, 2019; Simoncelli et al., 2020). Objects in the images (the labeled molecular entities) were detected or segmented, and then their colocalization was assessed based on their nearest neighbor distances. We took an object-based approach for two main reasons. First, for a basic measure of the extent of colocalization, the nearest neighbor distance allowed us to calculate the fraction of one object type colocalized with another object type (Mascalchi and Cordelieres, 2019). By interpreting colocalization fractions as probabilities, we then extended the analysis to calculate conditional probabilities and related measures that reflected the relationships between object colocalizations. Second, object-based analysis offered robust means to computationally assess the significance of any observed colocalization, a major challenge for colocalization analysis (Aaron et al., 2018; Costes et al., 2004). Specifically, in an object-based analysis it is relatively straightforward to (computationally) abolish the relationships between objects, e.g., by object randomization, while maintaining individual object integrity (Aaron et al., 2018; Fletcher et al., 2010; Lagache et al., 2015).

Throughout this work, we will employ the following terminology to refer to the three sets of objects, the colocalization relationships of which are being analyzed. The objects will be referred to as target (T), reference (R), and condition (C). The question that the analysis aims to answer is: How much is the colocalization of target objects with reference objects influenced by target and/or reference colocalization with condition objects? To answer this question, we employed a four-step analysis process. The below descriptions and derivations are for images containing diffraction-limited, punctate objects, the positions of which are described by their center coordinates. In the next section, we present an extension for non-punctate objects.

Step 1. Divide target and reference into groups colocalized or not colocalized with condition

Suppose there are N_T, N_R, and N_C target, reference, and condition objects, respectively (Fig. 1 A). First, we determined whether each target and reference object colocalized with a condition object (Fig. 1, A and B). This divided the objects into condition-positive groups (*TwC* and *RwC*; "w" indicates "with/positive") and condition-negative groups (*TnC* and *RnC*; "n" indicates "without/negative").

Two objects were considered colocalized when the distance between them was below a particular colocalization radius. The colocalization radius defined the spatial scale at which the colocalization relationships were explored. It also accounted for image properties such as localization precision (including imprecision introduced by the molecule labeling strategy [Bates et al., 2007]) and registration shifts between different channels. As will be shown later, performing conditional colocalization analysis using a range of colocalization radii yields more robust results than employing one colocalization radius.

The division of target and reference objects into condition-positive and condition-negative groups yielded the probability (p) of target and reference to colocalize with the condition:

$$p(TwC) = N_{TwC}/N_T, \quad (1)$$

$$p(RwC) = N_{RwC}/N_R, \quad (2)$$

where N_{TwC} and N_{RwC} are, respectively, the number of target objects and reference objects colocalized with condition objects (Fig. 1 B). These colocalization probabilities are equivalent to the colocalization measure in (Helmuth et al., 2010; where they are called "C^t").

Step 2. Calculate the fraction of target colocalizing with reference in the different group combinations

Next, we calculated the fractions of target objects in the different groups colocalized with reference objects in the different groups, also using the colocalization algorithm of Helmuth et al. (2010). As in Step 1, two objects were considered colocalized when the distance between them was below a particular colocalization radius. From this, we obtained five colocalization fractions (f_{coloc}): $f_{coloc}(TwR)$ (analysis of all target and reference; Fig. 1 C, top row), $f_{coloc}((TwC)wR)$ and $f_{coloc}((TnC)wR)$ (analysis focused on condition-positive and condition-negative target; Fig. 1 D), and $f_{coloc}(Tw(RwC))$ and $f_{coloc}(Tw(RnC))$ (analysis focused on condition-positive and condition-negative reference; Fig. 1 C).

For each colocalization fraction, we calculated a corresponding coincidental colocalization fraction in the absence of any true relationship between target and reference (f_{coloc}^{nullTR}). For this, we kept the reference objects in place and replaced the target objects with points on a grid within the cell area (Helmuth et al., 2010). Using the same colocalization radius as for the original data, we calculated f_{coloc}^{nullTR} corresponding to each of the colocalization fractions mentioned above. This procedure calculated the expected (coincidental) colocalization given the

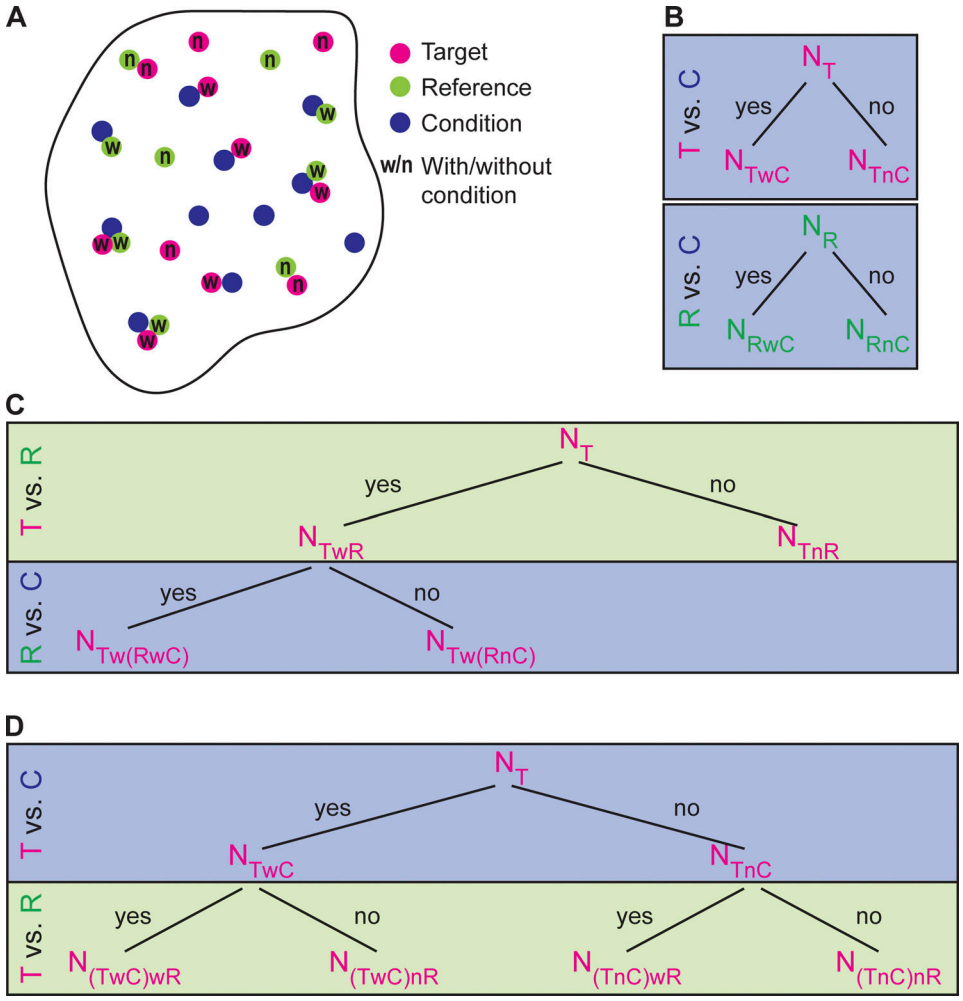

Figure 1. **Schematic and decision trees for classifying target and reference objects in terms of their colocalization with condition objects and with each other. (A)** Schematic of a "cell region" showing target (magenta) and reference (green) objects classified as with (w) or without (n) condition objects (blue). **(B)** Decision tree for dividing target (top) and reference (bottom) objects into two groups each based on their colocalization ("yes" branch) or not ("no" branch) with condition objects. **(C)** Decision tree for dividing target objects into colocalized or not with reference objects (top row; TwR and TnR), and then further dividing the relevant reference objects into colocalized or not with condition objects (bottom row; Tw(RwC) and Tw(RnC)). **(D)** Decision tree for dividing target objects into colocalized or not with condition objects (top row; a repeat of the decision tree in B, top), and then further dividing the condition-positive target objects (TwC) and condition-negative target objects (TnC) into colocalized or not with reference objects (bottom row; for condition-positive T: (TwC)wR and (TwC)nR; for condition-negative T: (TnC)wR and (TnC)nR.

number and spatial distribution of reference objects, i.e., it considered the spatial context of the colocalization analysis (Helmuth et al., 2010).

Step 3. Calculate conditional colocalization measures from colocalization fractions

The colocalization fractions obtained in Step 2 yielded five conditional colocalization measures:

Measure 1. The overall colocalization probability, $p(TwR)$:

The all target vs. all reference analysis (Fig. 1 C, top row) yielded the overall probability of the target to colocalize with reference, regardless of either's relationship to the condition.

$$p(TwR) = f_{coloc}(TwR) = N_{TwR}/N_T. \quad (3)$$

N_{TwR} = number of target objects colocalized with reference objects, irrespective of either's relationship to condition objects.

Measures 2 and 3. The influence of target colocalization with the condition on target colocalization with reference, $p(TwR|TwC)$ and $p(TwR|TnC)$:

The condition-positive and condition-negative target vs. all reference analyses (Fig. 1 D) yielded:

$$f_{coloc}((TwC)wR) = N_{(TwC)wR}/N_{TwC}, \quad (4)$$
$$f_{coloc}((TnC)wR) = N_{(TnC)wR}/N_{TnC}. \quad (5)$$

$N_{(TwC)wR}$ = number of target objects colocalized with both reference and condition objects. $N_{(TnC)wR}$ = number of target objects colocalized with reference objects but not with condition objects. N_{TwC} and N_{TnC} are from Step 1.

These fractions indicated the conditional probabilities of the target to colocalize with the reference given that the target is colocalized, or not colocalized, with the condition:

$$p(TwR|TwC) = p(TwR\&TwC)/p(TwC) \quad (6a)$$
$$= \left(N_{(TwC)wR}/N_T\right)/\left(N_{TwC}/N_T\right) \quad (6b)$$
$$= N_{(TwC)wR}/N_{TwC} = f_{coloc}((TwC)wR). \quad (6c)$$

Eq. 6a follows from the definition of conditional probability. Eq. 6b follows from the definition of $p(TwR\&TwC)$ for the numerator (Fig. 1 D, left branch) and Eq. 1 for the denominator. Eq. 6c follows from Eq. 4.

Similarly:

$$p(TwR|TnC) = p(TwR\&TnC)/p(TnC) \quad (7a)$$
$$= \left(N_{(TnC)wR}/N_T\right)/\left(N_{TnC}/N_T\right) \quad (7b)$$
$$= N_{(TnC)wR}/N_{TnC} = f_{coloc}((TnC)wR). \quad (7c)$$

Eq. 7a follows from the definition of conditional probability. Eq. 7b follows from the definition of $p(TwR\&TnC)$ for the numerator (Fig. 1 D, right branch) and the equivalent of Eq. 1 for TnC for the denominator. Eq. 7c follows from Eq. 5.

The comparison of $p(TwR|TwC)$, $p(TwR|TnC)$ and $p(TwR)$ assessed the extent to which target colocalization with reference was influenced by target colocalization with the condition.

Measures 4 and 5. The influence of reference colocalization with condition on target colocalization with reference ($p^{rs}(Tw(RwC))$ and $p^{rs}(Tw(RnC))$):

The all target vs. condition-positive and condition-negative reference analyses (Fig. 1 C, bottom row) yielded:

$$p(Tw(RwC)) = f_{coloc}(Tw(RwC)) = N_{Tw(RwC)}/N_T, \quad (8)$$
$$p(Tw(RnC)) = f_{coloc}(Tw(RnC)) = N_{Tw(RnC)}/N_T. \quad (9)$$

$N_{Tw(RwC)}$ = number of target objects colocalized with reference objects that are themselves colocalized with condition objects. $N_{Tw(RnC)}$ = number of target objects colocalized with reference objects that are not colocalized with condition objects.

As is, $p(Tw(RwC))$ and $p(Tw(RnC))$ could not be directly compared with $p(TwR)$ because the number of reference objects employed to calculate these different probabilities was different. Specifically:

$N_{RwC} + N_{RnC} = N_R$ (Fig. 1 B, bottom),
$N_{Tw(RwC)} + N_{Tw(RnC)} = N_{TwR}$ (Fig. 1 C, bottom row),
$p(Tw(RwC)) + p(Tw(RnC)) = p(TwR)$ (Eqs. 8 and 9 vs. Eq. 3).

In the absence of any special relationship between target objects and condition-positive or condition-negative reference objects, it follows from the above equations that:

$$p(Tw(RwC)) = p(TwR) \times p(RwC),$$
$$p(Tw(RnC)) = p(TwR) \times p(RnC) = p(TwR) \times (1 - p(RwC)).$$

Thus, we rescaled the colocalization probabilities:

$$p^{rs}(Tw(RwC)) = p(Tw(RwC))/p(RwC), \quad (10)$$
$$p^{rs}(Tw(RnC)) = p(Tw(RnC))/(1 - p(RwC)). \quad (11)$$

These measures could be >1, and thus they no longer indicated probabilities (unlike the original fractions in Eqs. 8 and 9). Nevertheless, rescaling factored out the number of reference objects used for analysis, allowing us to compare $p^{rs}(Tw(RwC))$, $p^{rs}(Tw(RnC))$ and $p(TwR)$ to assess the extent to which target colocalization with reference was influenced by reference colocalization with the condition.

In summary, Eqs. 3, 6, 7, 10, and 11 (in addition to Eqs. 1 and 2 in Step 1) provided us with useful measures for conditional colocalization analysis. Using f_{coloc}^{nullTR} instead of f_{coloc} in these equations yielded the coincidental counterparts of these measures in the absence of any true relationship between target and reference (p_{nullTR} and p^{rs}_{nullTR}). Conceptually, these measures explored different facets of the joint probability distribution describing the colocalization of the target, reference, and condition (see Materials and methods, Eqs. 12, 13, 14, 15, 16, 17, 18, 19, 20, 21, 22 and related text) to address the specific question of how much the condition influences target-reference colocalization (which the joint distribution, as is, does not).

Step 4. Assess significance of the condition's influence by randomizing condition locations

The nullTR counterparts of the conditional colocalization measures assessed their coincidental values in the absence of a true relationship between target and reference. Similarly, it was important to assess their coincidental counterparts in the absence of any true influence of the condition on target colocalization with reference. For this, we randomized the locations of the condition objects, while keeping the same number of condition objects and not altering the target or reference in any way (see Materials and methods and Fig. S1, A–F). We performed the condition object randomization 100 times for robustness (Fig. S1 G). For each randomization instance, we repeated Steps 1–3 and calculated the coincidental colocalization measures corresponding to that instance. Averaging over the 100 randomization instances then yielded the final coincidental colocalization measures (p_{randC} and p^{rs}_{randC}), which were compared with the original data colocalization measures. This allowed us to assess the significance of any revealed influence of the condition on target colocalization with reference.

Generalization of conditional colocalization analysis to non-punctate objects

In the above analysis scheme, we assumed that objects were diffraction-limited puncta and defined the distance between them as the distance between their center coordinates. While this covers many colocalization questions, many subcellular structures of interest, especially as condition objects, could be larger. Therefore, we generalized the above scheme to the case of non-punctate objects through three modifications. First, we replaced Gaussian fitting with image segmentation to delineate non-punctate objects. Second, to calculate the coincidental colocalization fraction ("nullTR" in Step 2 above) for non-punctate target objects, we employed 100 randomizations of the target objects instead of a grid to preserve the nature of target objects (Fig. S1 H). Third, we generalized the definition of distance between objects by defining the colocalization distance from object A to object B as the average (Euclidean) distance from every pixel in object A to the nearest pixel in object B (Fig. S2).

With this definition, the colocalization distance for two punctate objects was the Euclidean distance between their positions, as above. For the case of the distance from a punctate object to a non-punctate object, the colocalization distance was the distance from the position of the punctate object to the closest pixel of the non-punctate object. Note that the colocalization distance defined as such was not symmetric: the

colocalization distance from A to B was not necessarily the same as the colocalization distance from B to A. This was because the colocalization distance considered the shapes and sizes of non-punctate objects in addition to their relative locations, all of which were relevant for the assessment of colocalization (Bolte and Cordelières, 2006; Lachmanovich et al., 2003; Fig. S2). While other metrics could be employed to assess colocalization between non-punctate objects, such as the fraction of area overlap (Mascalchi and Cordelieres, 2019), an advantage of the colocalization distance as defined here was that it was equally applicable to punctate and non-punctate objects. With these modifications, the conditional colocalization analysis scheme was applicable to punctate and non-punctate objects and their combinations.

Analysis accurately estimates conditional colocalization measures in simulated data

To assess the accuracy of our conditional colocalization analysis scheme, we tested it on simulated data with known ground-truth colocalization measures. To make the simulations realistic, we took experimental data cell masks and simulated various colocalization scenarios within them. To localize punctate objects, we selected sub-pixel coordinates within each cell mask. For non-punctate objects, we either used paxillin patch segmentations from our experimental data or generated non-punctate objects of similar size and shape to the paxillin patch segmentations (Fig. S3, A–C).

First, we validated the core colocalization analysis between two sets of objects covering three scenarios: (i) punctate target and reference, (ii) punctate target and non-punctate reference, and (iii) non-punctate target and reference. We employed multiple parameter combinations (described in detail in Materials and methods), each simulated 28 times (scenarios i and ii) or 15 times (scenario iii) using 28 or 15 cell masks, respectively. In scenarios i and ii (Fig. 2, A and B), using a colocalization radius of three pixels (which was compatible with how the simulated data were generated), the calculated $p(TwR)$ for each parameter combination was very close to its ground-truth value, and, as expected, it was independent of N_T and N_R. Also as expected, the coincidental colocalization probability $p_{nullTR}(TwR)$ depended only on N_R, reflecting the fraction of the cell mask area covered by the colocalization zones around the reference objects. In scenario (iii), using a colocalization radius of three pixels, the calculated $p(TwR)$ and $p_{nullTR}(TwR)$ were close to their input/expected values, but they were overall slightly underestimated (Fig. 2 C). We reasoned that this was because the employed colocalization radius was too small relative to the size of the simulated target objects. Indeed, rerunning the colocalization analysis using a radius of six pixels yielded more accurate $p(TwR)$ estimates, although with a concomitant increase in $p_{nullTR}(TwR)$ (Fig. S3 D). These results highlight how the colocalization distance between non-punctate objects reflects both their distance and size/shape (Fig. S2), and thus the colocalization radius must take these object properties into account.

Next, we validated the conditional colocalization analysis of three sets of objects. We tested three scenarios: (i) all objects were punctate, (ii) the target and reference were punctate while the condition was non-punctate, and (iii) all objects were non-punctate. For each scenario, we employed multiple parameter combinations (described in detail in Materials and methods), each simulated 15 times using 15 cell masks. We then performed conditional colocalization analysis using a colocalization radius of three pixels. We compared the calculated $p(TwC)$, $p(RwC)$, $p(TwR|TwC)$ and $p(TwR|TnC)$ to their input values, and the calculated $p(TwR)$, $p^{rs}(Tw(RwC))$ and $p^{rs}(Tw(RnC))$ to their expected values (Eqs. 23, 24, and 25).

We found that the conditional colocalization measures were estimated accurately for all scenarios, with a slightly worse performance in scenario iii (Fig. 2, D–G). As expected, all conditional colocalization measures were higher than their corresponding nullTR, reflecting the simulated colocalization relationships. All nullTR values were very similar to each other, demonstrating that the rescaling employed to calculate $p^{rs}(Tw(RwC))$ and $p^{rs}(Tw(RnC))$ (Eqs. 10 and 11) properly factored out the number of reference objects used for analysis, placing all colocalization measures on the same scale for direct comparison. Also as expected, $p(TwR)$ was the "weighted average" of $p(TwR|TwC)$ and $p(TwR|TnC)$, with the weights given by $p(TwC)$ and $p(TnC)$ (Eq. 23). Of note, the randC equivalent of all conditional colocalization measures had a median value very close to $p(TwR)$. This was because, upon condition object randomization, the randC condition-positive and condition-negative groups of target and reference were, in fact, random subsets of target and reference objects, yielding randC conditional colocalization measures that converged to $p(TwR)$. The true ("Data") conditional colocalization measures were then higher or lower than their corresponding randC values, depending on the specific simulated scenario. All in all, these results demonstrate that our analysis scheme accurately estimates relevant conditional colocalization measures for both punctate and non-punctate objects.

Analysis over a range of colocalization radii robustly reveals colocalization relationships

A critical parameter for conditional colocalization analysis is the colocalization radius. As discussed above, for the analysis of non-punctate target and reference objects, it must account for their size. But even for punctate objects, it must accommodate properties of the images, such as localization precision, registration shifts between channels, and the labeling density of molecules and complexes. As a result, and especially in conventional light microscopy, the colocalization radius is in the tens to hundreds of nanometers, which is large compared to molecular dimensions. Therefore, it is important to determine the influence of the colocalization radius on conditional colocalization analysis and to determine strategies for obtaining robust, sensitive, and specific analysis results.

To investigate this, we applied our analysis to molecules known to interact with each other (positive control) and to molecules not known to interact with each other (negative control). For the positive control, we chose three proteins that are part of focal adhesions (FAs), namely (activated) β_1-integrin, (phosphorylated) focal adhesion kinase (pFAK), and paxillin (Geiger et al., 2009; Vicente-Manzanares and Horwitz, 2011).

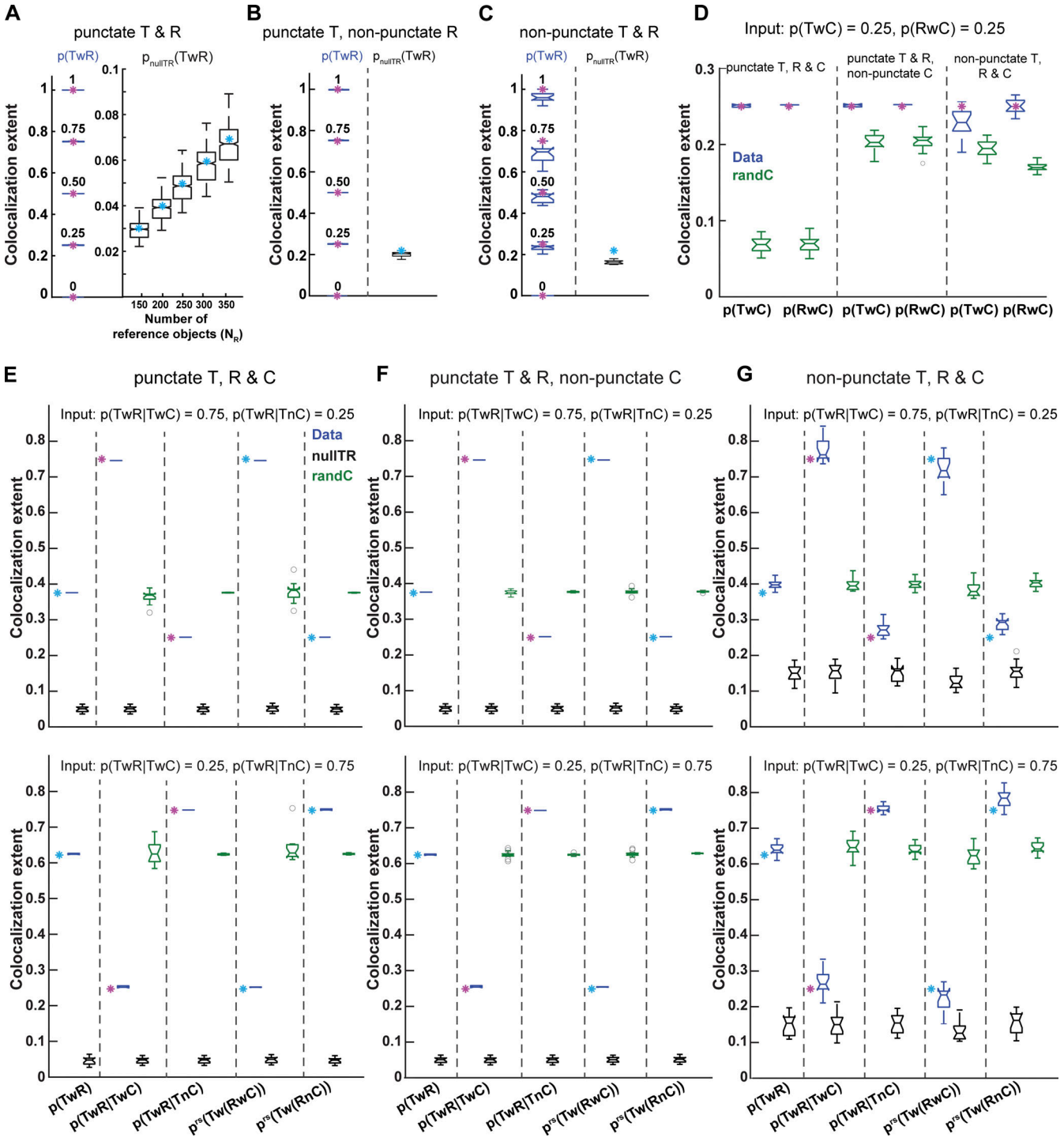

Figure 2. **Analysis scheme accurately estimates conditional colocalization measures. (A–C)** Calculated $p(TwR)$ (left) and corresponding $p_{nullTR}(TwR)$ (right) for simulations of the indicated target and reference object types. Each box shows the calculated values for all parameter combinations using the same input $p(TwR)$ or having the same expected $p_{nullTR}(TwR)$. Input/expected values are shown as magenta/cyan asterisks. For each box (also applicable to D–G), the central mark is the median, the edges are the 25th and 75th percentiles, and the dashed whiskers extend to the most extreme inlier data points. Dots indicate outlier datapoints (as deemed by the Matlab "boxplot" function). Notch around median indicates the 95% confidence interval of the median. In A, each box represents N = 700 values (25 N_T and N_R combinations [left], or 25 N_T and $p(TwR)$ combinations [right], each repeated 28 times). In B, each $p(TwR)$ box represents N = 140 values (5 N_T values, each repeated 28 times), while the $p_{nullTR}(TwR)$ box represents N = 700 values (25 N_T and $p(TwR)$ combinations, each repeated 28 times). In C, each box represents N = 15 values (15 repeats for each $p(TwR)$). **(D–G)** Representative results of calculated conditional colocalization measures. Each box represents N = 15 repeats of the stated simulation parameters. **(D)** Calculated $p(TwC)$ and $p(RwC)$ and their "randC" counterparts for the indicated object type combinations. Simulation parameters: $p(TwR|TwC)$ = 0.75, $p(TwR|TnC)$ = 0.25, $p(TwC)$ = $p(RwC)$ = 0.25. Input values are shown as magenta asterisks. **(E–G)** Calculated conditional colocalization measures and their "nullTR" and "randC" counterparts for the indicated object type combinations and indicated $p(TwR|TwC)$ and $p(TwR|TnC)$ values (together with $p(TwC)$ = $p(RwC)$ = 0.25). Input/expected values are shown as magenta/cyan asterisks (see Materials and methods for details). In G, nullTR was calculated using 50 target randomizations instead of 100 for computational efficiency.

Paxillin was taken as a marker for FAs, which served as condition objects. As pFAK interacts with cell surface receptors other than integrins and is involved in signaling pathways other than FA formation (Marlowe et al., 2016; Murphy et al., 2019; Rigiracciolo et al., 2019; Sulzmaier et al., 2014), we reasoned that conditional colocalization analysis may reveal differential colocalization between β_1-integrin and pFAK at FAs vs. away from FAs. For the negative control, we chose the transferrin receptor (TfR), the adaptor protein TSAd (T cell specific adaptor), and clathrin heavy chain (CHC). There are no reports of association between TfR and TSAd. At the same time, CHC is a marker for clathrin-coated structures (CCSs), which mediate TfR internalization into the cell (Liu et al., 2010; Mayle et al., 2012). Thus, we would expect a certain level of association between TfR and CCSs, making them relevant condition objects.

We performed three-color immunofluorescence (IF) imaging of the two combinations of molecules in endothelial cells (ECs) using total internal reflection fluorescence microscopy (TIRFM). This allowed us to focus on the bottom cell surface and minimize apparent colocalization from signals existing in different *z*-planes (Figs. 3 A and S4 A). For images with a punctate nature (all but paxillin), we determined object positions with subpixel localization using Gaussian fitting (Aguet et al., 2013; Jaqaman et al., 2008; Fig. 3, B and C; and Fig. S4, B–E). For the paxillin images, we segmented the paxillin patches using intensity-based thresholding (Jaqaman et al., 2016), focusing on objects larger than the diffraction limit (Fig. 3, D and E). The punctate nature of target and reference in these datasets allowed us to investigate the effect of the colocalization radius on our analysis results in the worst-case scenario, where the colocalization radius is 1–2 orders of magnitude larger than the object dimensions.

We then performed conditional colocalization analysis using a range of colocalization radii, namely 1–6 pixels (81–486 nm). Throughout this study, we will present the analysis results in two ways. First, as boxplot graphs of the colocalization measures and their coincidental counterparts (nullTR and/or randC), showing individual cell measurements (Fig. 3, F and G). Second, as $-\log_{10}$(P value) tables, summarizing the results of the statistical tests assessing the significance of the observed colocalization measures (Fig. 3 H). For $p(TwR)$, the listed P value is that for comparing $p(TwR)$ to its corresponding nullTR. If $p(TwR)$ is significantly greater/less than its corresponding nullTR, it indicates significant colocalization/repulsion. For all other measures in the table, three tests were performed to assess significance, namely comparison to nullTR, randC and $p(TwR)$. A measure indicates significantly increased/decreased colocalization relative to overall colocalization if it is significantly higher/lower in all three comparisons (using the Dunn–Sidak correction to control for the total type-I error). Thus, the table lists the least significant P value (the smallest $-\log_{10}$(P value)) among the three tests for each measure. Below, we summarize our main findings from applying conditional colocalization analysis to the positive and negative control datasets.

Analysis is specific

In the positive control dataset, activated β_1-integrin and pFAK exhibited significant colocalization with the paxillin patches (representing FAs, the condition objects; Fig. 3 F). Conditional colocalization analysis also identified robust colocalization relationships between β_1-integrin and pFAK in the context of FAs over the employed range of colocalization radii (Fig. 3, G–J; to be discussed next). In stark contrast, in the negative control dataset, no colocalization relationships were identified between TfR and TSAd, even though both exhibited significant colocalization with CHC (representing CCSs, the condition objects; Fig. S4, F and G). This demonstrates a high level of specificity in the analysis, up to a colocalization radius of at least 6 pixels (486 nm), which we attribute largely to the statistics-based assessment of coincidental colocalization (nullTR and randC).

Analysis reveals differential colocalization for different molecule subsets

Conditional colocalization analysis revealed that β_1-integrin and pFAK exhibited significant colocalization with each other, mainly for the subset of pFAK colocalized with paxillin. When investigating the fraction of β_1-integrin (target) colocalized with pFAK (reference), $p^{rs}(Tw(RwC))$ was significantly higher than its coincidental counterparts and $p(TwR)$ at all colocalization radii, indicating that β_1-integrin colocalized significantly more with the paxillin-positive pFAK subset than with pFAK overall (Fig. 3, G–I). Conversely, when investigating the fraction of pFAK (target) colocalized with β_1-integrin (reference), $p(TwR|TwC)$ was significantly higher than its coincidental counterparts and $p(TwR)$ at all colocalization radii, indicating that the paxillin-positive pFAK subset colocalized significantly more with β_1-integrin compared with overall pFAK (Fig. 3 J). In contrast to the strong colocalization observed between β_1-integrin and the paxillin-positive subset of pFAK, the overall colocalization between β_1-integrin and pFAK was much weaker: pFAK colocalization with β_1-integrin was not significant at any colocalization radius ($p(TwR)$ in Fig. 3 J), while β_1-integrin colocalization with pFAK was borderline significant at colocalization radii ≥3 pixels ($p(TwR)$ in Fig. 3 H).

These results demonstrate the sensitivity of conditional colocalization analysis and its ability to reveal differential colocalization for different molecule subsets, reflecting the heterogeneity in their interaction landscape. They also highlight how identifying the proper subset of pFAK—that colocalized with FAs—is critical for capturing the strong colocalization relationship between pFAK and β_1-integrin, as pFAK not at FAs is most likely interacting with other receptors (Sulzmaier et al., 2014).

True colocalization relationships appear over a range of colocalization radii

While the colocalization between β_1-integrin and the paxillin-positive subset of pFAK was significant at all colocalization radii, the level of significance varied with colocalization radius in a systematic manner: initially, it increased with colocalization radius, reaching a peak/plateau at colocalization radius of 3–4 pixels, and then it decreased as the colocalization radius increased further (reflected in the increase and then decrease of the $-\log_{10}$(P value) of $p^{rs}(Tw(RwC))$ in Fig. 3 H and of $p(TwR|TwC)$ in Fig. 3 J, bottom). The lower significance levels for

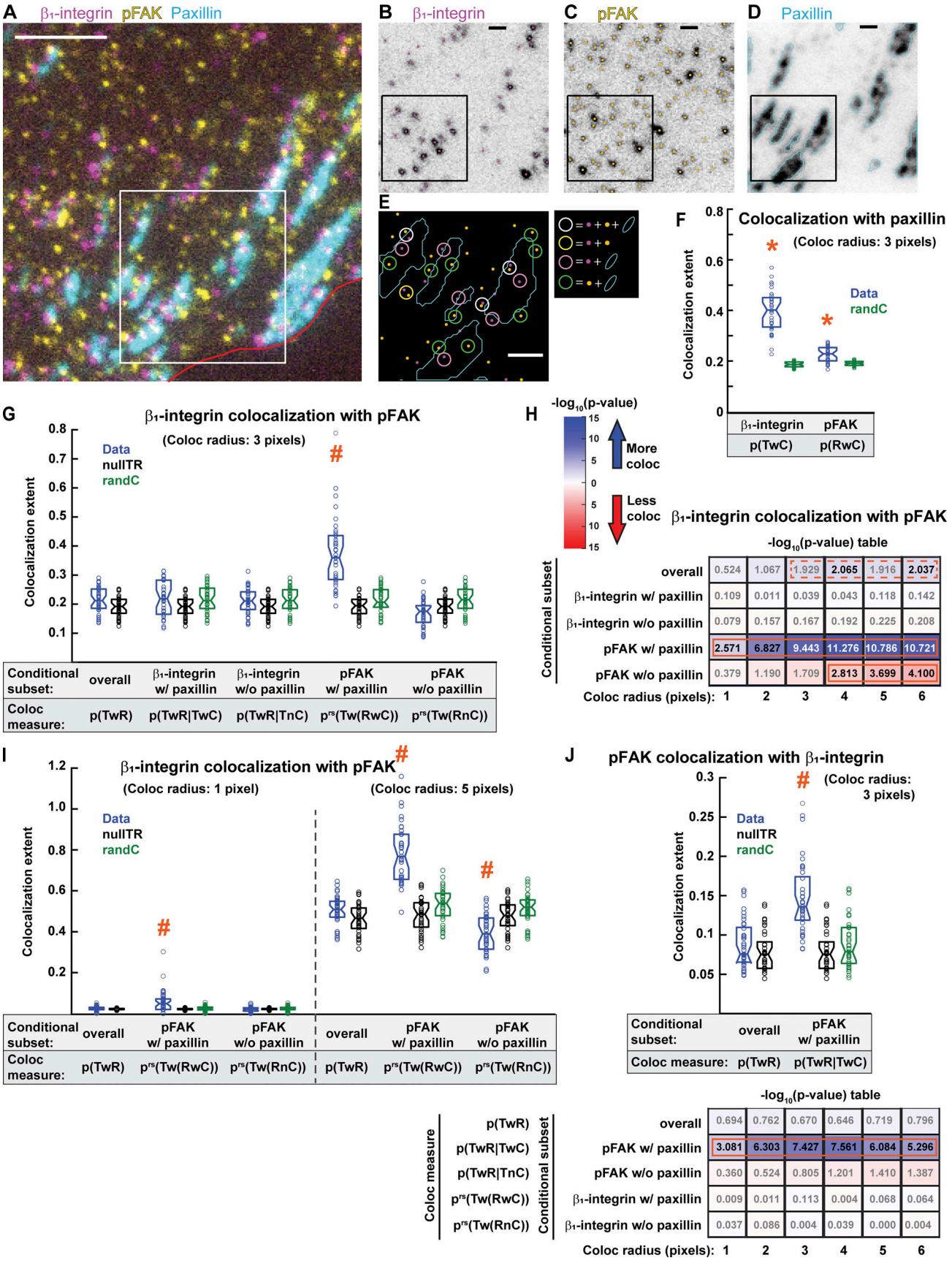

Figure 3. **Conditional colocalization analysis captures the colocalization relationships of an experimental positive control. (A)** Representative three-color IF image of activated β_1-integrin, pFAK and paxillin on the surface of a TIME cell imaged via TIRFM. The red line shows the cell edge. Scale bar, 5 µm.

(B–D) Particle detections (shown as dots in B and C) and patch segmentation (shown as outlines in D) overlaid on the individual channels for the area within the white box in A. Scale bar, 1 µm. **(E)** Overlay of the three-channel detections and segmentations for the area within the black box in B–D, with color coding following that in B–D. Colored circles (diameter = 243 nm) point out colocalization events between the different molecules, following color-coding in the legend on the side. Scale bar, 1 µm. **(F)** Probabilities of β_1-integrin and pFAK to colocalize with the condition (paxillin; representing FAs), together with their coincidental counterparts ("randC"), using the indicated colocalization radius. The x-axis indicates above each colocalization measure the molecule that it represents. For each box, individual dots indicate individual cell measurements, the central mark is the median and the edges are the 25th and 75th percentiles. Notch around median indicates the 95% confidence interval of the median. Dots with same color as box are inliers and gray dots are outliers (as deemed by the Matlab "boxplot" function). *: P < 0.01, indicating that the probability of colocalization with condition is significantly greater than its coincidental counterpart, as assessed via a Wilcoxon rank-sum test. **(G)** Conditional colocalization measures and their coincidental counterparts ("nullTR" and "randC"), using the indicated colocalization radius, for target = β_1-integrin, reference = pFAK and condition = paxillin. The x-axis indicates above each colocalization measure the molecule subset that it represents. Boxplots and dots as in F. #: colocalization measure is significant, i.e., it is significantly greater than its coincidental counterparts (both "nullTR" and "randC") and $p(TwR)$, as assessed via three Wilcoxon rank-sum tests. The significance threshold for each individual test is calculated using the Dunn–Sidak correction to give a total type-I error rate (for all three tests) of 0.05. **(H)** $-\log_{10}$(P value) table summarizing the significance of each conditional colocalization measure (see text for details) at the indicated colocalization radii, for target = β_1-integrin, reference = pFAK and condition = paxillin. The correspondence between indicated molecule subsets and colocalization measures is same as in G. For $p(TwR)$ ("overall"), blue/red indicates greater than/less than the corresponding "nullTR". For all other measures, blue/red indicate greater than/less than $p(TwR)$. Intensity of color increases as significance increases, as shown in color bar. Values in black or white are significant, values in gray are not significant. Table entries with solid red outline highlight significant colocalization measures over a range of colocalization radii. Table entries with dashed red outline highlight borderline significant colocalization measure over a range of colocalization radii. **(I)** Conditional colocalization measures as in G, but at indicated colocalization radii. Only significant conditional colocalization measures, together with $p(TwR)$, are shown. All details are as in G. **(J)** Conditional colocalization measures and their coincidental counterparts (top) and $-\log_{10}$(P value) table summarizing the significance of each conditional colocalization measure (bottom), at the indicated colocalization radii, for target = pFAK, reference = β_1-integrin and condition = paxillin. Only significant conditional colocalization measures, together with $p(TwR)$, are shown in boxplot form. Boxplot graph details as in G. The $-\log_{10}$(P value) table indicates next to each colocalization measure the molecule subset that it represents. Other details as in H. *N* = 37 cells from four repeats. See Table 3 for number of objects per channel and other dataset properties.

smaller colocalization radii were probably due to higher levels of false negatives in the colocalization classification (as observed in Fig. 2 C). For larger colocalization radii, lower significance levels were probably due to higher levels of false positives and overestimation of coincidental colocalization (nullTR and randC). An intermediate colocalization radius of 3–4 pixels offered the best balance between false positives and false negatives for this dataset, providing the highest level of significance.

As the optimal colocalization radius is generally not known *a priori*, these results suggest that analyzing the data using a range of colocalization radii is the optimal strategy for robust colocalization analysis. True colocalization relationships are expected to appear as significant over a range of radii (not necessarily the full range employed), with a pattern of increasing and then decreasing significance as the radius changes from small to optimal to large. This criterion for identifying meaningful colocalization relationships also safeguards against the spurious identification of colocalization relationships at isolated colocalization radii (i.e., not a continuous range of radii) due to the increased false-positive rate associated with multiple statistical tests (Farcomeni, 2008).

Different colocalization measures reveal complementary aspects of the colocalization relationships

Complementary to the strong colocalization observed between β_1-integrin and paxillin-positive pFAK, our analysis revealed a substantial lack of colocalization between β_1-integrin and the paxillin-negative subset of pFAK ($p^{rs}(Tw(RnC))$ in Fig. 3, G–I and $p(TwR|TnC)$ in Fig. 3 J). The colocalization for this subset was less than its coincidental counterparts and $p(TwR)$. The reduction in colocalization was more apparent for larger colocalization radii (Fig. 3, H and J), probably because, at larger colocalization radii, the pFAK objects making the paxillin-negative subset were further away from FAs. These observations further emphasize the benefit of performing conditional colocalization analysis using a range of colocalization radii, allowing for the analysis of different subsets of target and reference objects. They also suggest that consistent, complementary trends for complementary colocalization measures (e.g., increased $p(TwR|TwC)$ is consistent with decreased $p(TwR|TnC)$, and similarly for $p^{rs}(Tw(RwC))$ vs. $p^{rs}(Tw(RnC))$) enhance the evidence for the revealed colocalization relationships.

Analysis yields consistent results for high and low signal-to-noise ratio images

The accuracy of our conditional colocalization analysis is expected to depend on the accuracy of the object detections and/or segmentations, which in turn depend on the images' signal-to-noise ratio (SNR). Therefore, we investigated the performance of conditional colocalization analysis for images with different SNR.

We took the positive control dataset, which had an SNR in the range of 4–10 (see Materials and methods for definition of SNR) and added Gaussian white noise to the images in order to reduce the SNR to 4, 3, and 2 (Materials and methods; Fig. 4 A). After detecting and segmenting the images as above, we performed conditional colocalization analysis (using a colocalization radius of three pixels) and compared the results at lower SNR to those of the original images (Fig. 4, B and C). We found that colocalization between β_1-integrin and the paxillin-positive subset of pFAK was captured at all tested SNRs. However, the significance of $p^{rs}(Tw(RwC))$ exhibited a decreasing trend as the SNR was reduced. This implies that, for weaker colocalization relationships, the relevant colocalization measures may lose significance at lower SNRs.

The comparisons also revealed that all measures, together with their coincidental counterparts, decreased with decreasing SNR (Fig. 4 B). This was because, at lower SNR, a smaller number of objects was detected in each channel, as only brighter

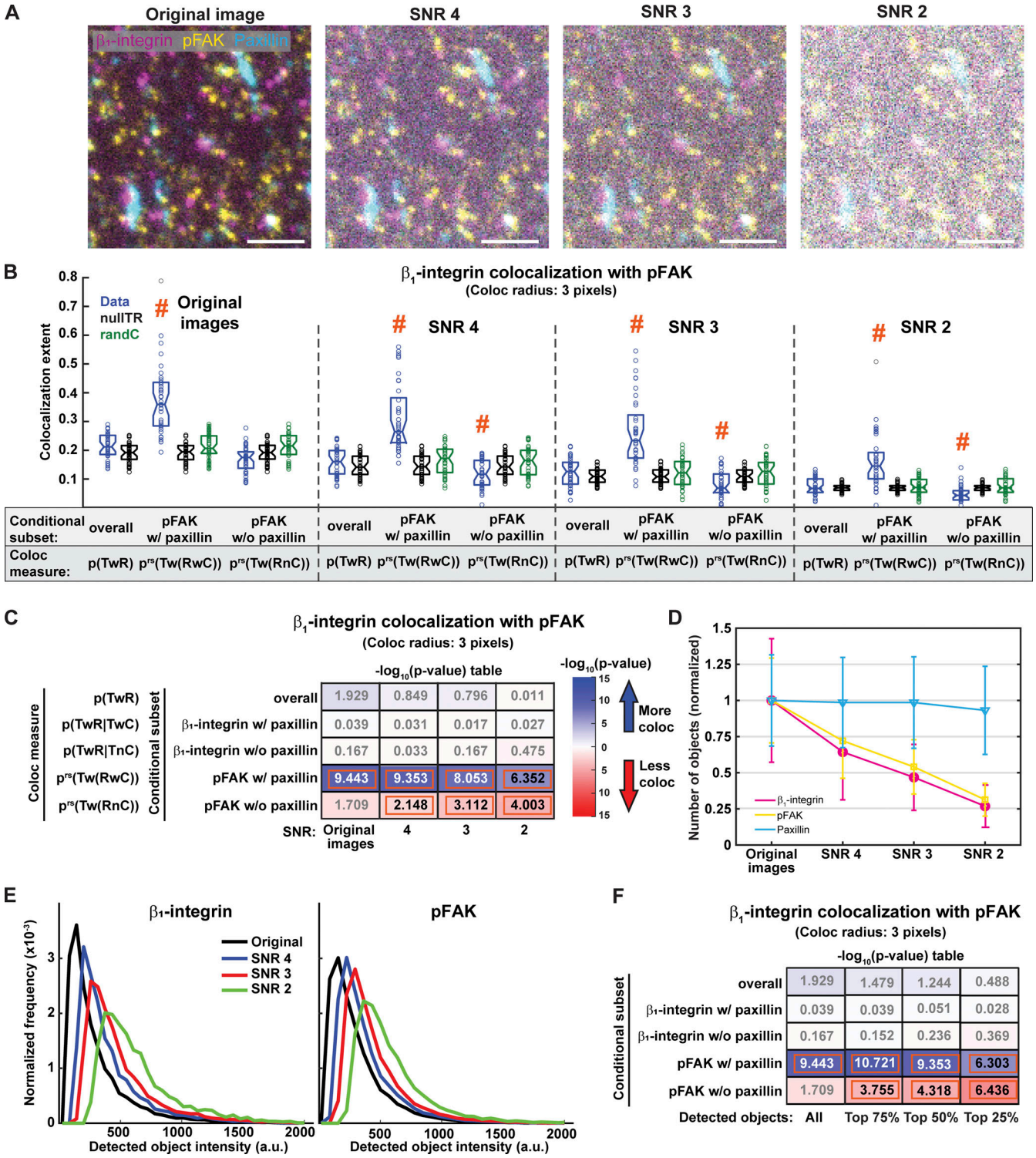

Figure 4. **Conditional colocalization analysis is robust with respect to image noise. (A)** Representative three-color IF image of activated β_1-integrin, pFAK and paxillin on the surface of a TIME cell imaged via TIRFM, before and after adding increasing levels of noise to lower the image SNR to indicated levels. Scale bar, 5 µm. **(B and C)** Conditional colocalization measures and their coincidental counterparts ("nullTR" and "randC"; B) and $-\log_{10}$(P value) table summarizing the significance of each conditional colocalization measure (see text for details; C) for target = β_1-integrin, reference = pFAK and condition = paxillin, as derived from images with the indicated SNR (all using a colocalization radius of 3 pixels). In B, only significant conditional colocalization measures, together with *p*(*TwR*), are shown. Details as in Fig. 3 G. In C, the $-\log_{10}$(P value) table indicates next to each colocalization measure the molecule subset that it represents. Other details as in Fig. 3 H. **(D)** Number of detected (β_1-integrin and pFAK) or segmented (paxillin) objects in each of the three channels at the different SNRs, normalized to the mean number of objects in the original images, shown as mean ± SD. **(E)** Intensity distribution of detected β_1-integrin and pFAK objects in the original images and in the images with added noise. **(F)** $-\log_{10}$(P value) table summarizing the significance of each conditional colocalization measure as calculated from the complete set of detections or after retaining only the top 75, 50 and 25% brightest objects among the β_1-integrin and pFAK detections. The correspondence between indicated molecule subsets and colocalization measures is same as in C. Other details as in Fig. 3 H. *N* and dataset properties as in Fig. 3.

objects were detectable above the noise level (Fig. 4, D and E). Also, an additional conditional colocalization measure, $p^{rs}(Tw(RnC))$, became significant at lower SNR (Fig. 4, B and C). This trend was also most likely because of the retention of only brighter objects at lower SNR; performing conditional colocalization analysis on the original data, but taking only the top 75, 50, and 25% brightest objects, revealed the same trend (Fig. 4 F). The significant $p^{rs}(Tw(RnC))$ indicated that β_1-integrin was less likely to colocalize with paxillin-negative pFAK than with the overall, complementing the significant preferential colocalization of β_1-integrin with paxillin-positive pFAK, as observed for the original data at colocalization radii ≥4 pixels (Fig. 3 H).

Overall, these results demonstrate that conditional colocalization analysis has the sensitivity to identify colocalization relationships at SNRs as low as 2. Nevertheless, imaging conditions that maximize the completeness and accuracy of detection/segmentation of the objects of interest will ensure maximal sensitivity and accuracy of the conditional colocalization analysis results.

Application: Conditional colocalization analysis reveals differential receptor-downstream adaptor colocalization relationships at different membrane locations

The spatial compartmentalization of molecular interactions is an emerging theme in signaling. For example, cell surface receptors have been observed to preferentially interact with downstream effectors at particular membrane microdomains and to signal differently from different subcellular compartments (Birch et al., 2021; Delos Santos et al., 2015; Eichmann and Simons, 2012; Jaqaman and Ditlev, 2021; Sorkin and von Zastrow, 2009; Sungkaworn et al., 2017). As a result, there is increasing interest in characterizing the spatial variation of colocalization between molecules within the cell (Gorlewicz et al., 2020; Jaskolski et al., 2005; Taylor et al., 2018). Conditional colocalization analysis is ideally suited to shed light on the spatial regulation and/or compartmentalization of molecular interactions within their cellular environment in an automated and quantitative fashion.

To illustrate this capability, we applied conditional colocalization analysis to the receptor tyrosine kinase VEGFR-2 (Vascular Endothelial Growth Factor Receptor 2) and its downstream adaptor TSAd (also known as VEGF receptor adaptor protein [VRAP]), in the context of FAs and CCSs (Figs. 5 and 6). VEGFR-2, expressed on the surface of ECs, is the main receptor for VEGF (short for VEGF-A), where it initiates signaling pathways that are essential for vascular function (Ferrara et al., 2003; Simons et al., 2016). Its downstream adaptor TSAd mediates a signaling cascade that modulates FA turnover and cell adhesion, critically important for EC motility and angiogenic sprouting (Abedi and Zachary, 1997; Birukova et al., 2009; Gordon et al., 2016; Sun et al., 2012; Wu et al., 2000). Interestingly, IF imaging of VEGFR-2 and paxillin (as a marker for FAs) indicated that a subset of VEGFR-2 tends to localize at/near FAs (Fig. 5 A), raising the possibility that this facilitates VEGFR-2–TSAd interactions to regulate FAs. As for CCSs, VEGFR-2 is internalized from the cell surface via clathrin-mediated endocytosis, in both ligand-independent and ligand-dependent manners, where it can continue downstream signaling (Basagiannis et al., 2016; Lampugnani et al., 2006; Lanahan et al., 2010; Simons et al., 2016). Thus, VEGFR-2 is also expected to colocalize with CCSs, potentially together with TSAd. Conditional colocalization analysis allowed us to investigate the colocalization relationships between VEGFR-2 and TSAd in the context of these two functionally-relevant membrane domains.

We performed three-color IF imaging of VEGFR-2, TSAd, and paxillin or VEGFR-2, TSAd, and CHC using TIRFM, in the absence or presence of 2 nM VEGF (5 min stimulation before fixation, enough for VEGFR-2 activation [da Rocha-Azevedo et al., 2020]) (Figs. 5 A and 6 A). As above, punctate signals (all but paxillin) were localized using Gaussian fitting (Aguet et al., 2013; Fig. 5, B and C; and Fig. 6, B–E), while paxillin patches were segmented using intensity-based thresholding (Jaqaman et al., 2016; Fig. 5, D and E). We then performed conditional colocalization analysis using a range of colocalization radii (1–6 pixels, as above).

First, we measured the extent of VEGFR-2 and TSAd colocalization with FAs, and whether they depended on each other (in a statistical sense) for FA colocalization. Taking VEGFR-2 as the target, FAs as the reference, and TSAd as the condition, only $p(TwR)$ was significant (Fig. 5 F; median value of $p(TwR)$ using a colocalization radius of 3 pixels = 0.27). This was at all colocalization radii, in both the absence and presence of VEGF. This indicated strong colocalization of VEGFR-2 with FAs, regardless of whether VEGFR-2 was colocalized with TSAd, and regardless of stimulation with VEGF. In contrast, taking TSAd as target and VEGFR-2 as the condition (while keeping FAs as reference), we found that $p(TwR)$ was largely not significant, while $p(TwR|TwC)$ was significantly greater than its counterparts for a range of radii, and $p(TwR|TnC)$ was significantly lower than its counterparts for larger radii (as observed for the positive control; Fig. 5, G and H). In addition, $p(TwR|TwC)$ had more significant P values and for a larger range of colocalization radii in the presence of VEGF vs. its absence (Fig. 5 H). These results indicated that only the VEGFR-2-positive subset of TSAd colocalized with FAs, with an increase in colocalization upon stimulation with VEGF. They suggest that VEGFR-2 plays a role in recruiting and/or retaining TSAd at FAs, and that this is enhanced upon VEGFR-2 activation (which promotes VEGFR-2–TSAd interactions).

What about VEGFR-2-TSAd colocalization? Is it influenced by location relative to FAs? For this, we used FAs now as the condition, and then once VEGFR-2 as target and TSAd as reference, and once the converse. In both cases, VEGFR-2-TSAd colocalization was only significant for the subset of TSAd colocalized with FAs ($p^{rs}(Tw(RwC))$ in Fig. 5 I and $p(TwR|TwC)$ in Fig. 5 J). The colocalization between VEGFR-2 and the FA-positive subset of TSAd was stronger upon VEGF stimulation than in its absence (more significant P values for a larger range of colocalization radii). These results suggest that not only does VEGFR-2 play a role in TSAd colocalization with FAs, but also FAs play a role in TSAd–VEGFR-2 colocalization. In other words, there appears to be cooperativity in the colocalization of TSAd with VEGFR-2 and FAs.

As for CCSs, conditional colocalization analysis revealed a different interplay between them and VEGFR-2–TSAd

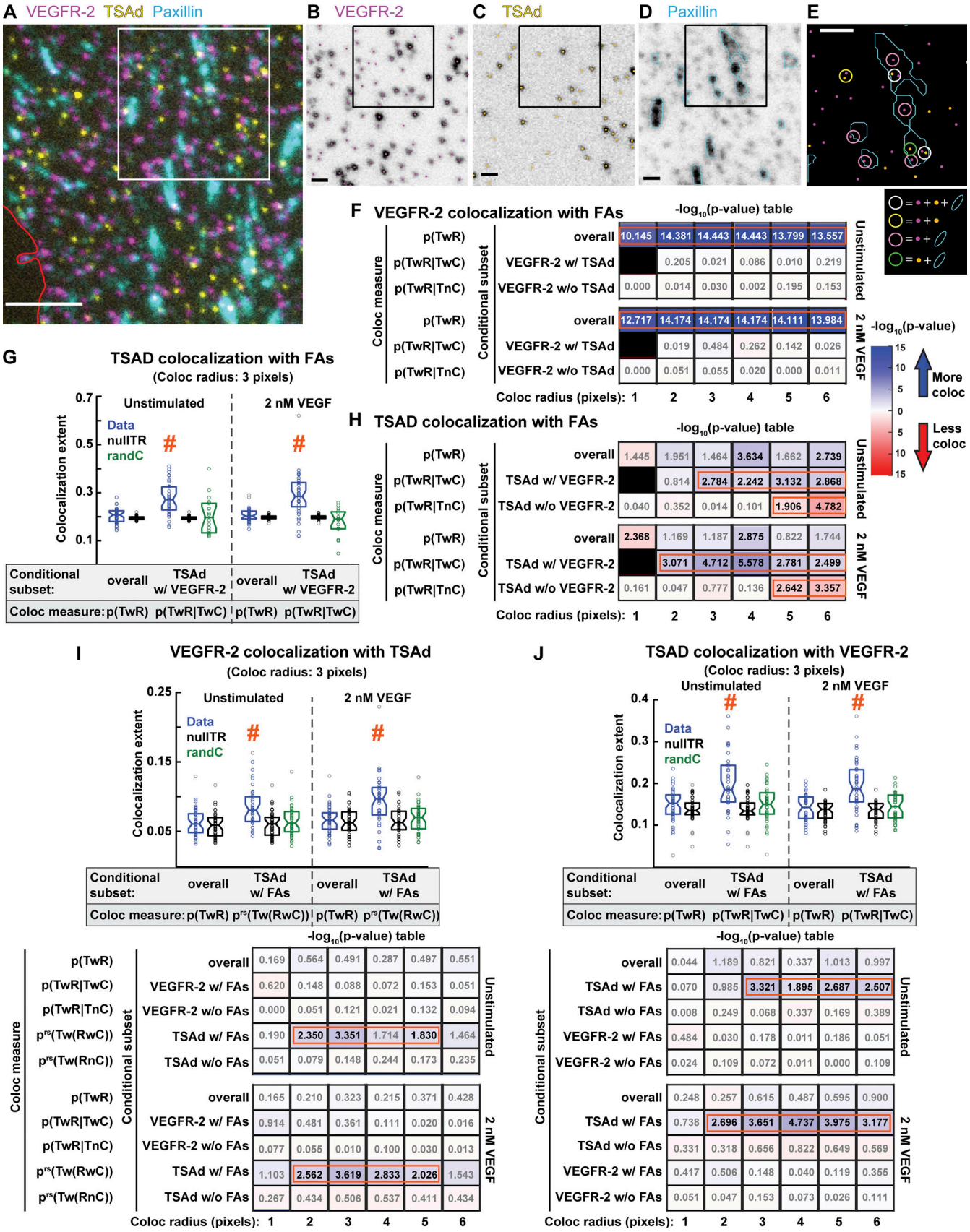

Figure 5. **TSAd-VEGFR-2 and TSAd-FA colocalization mutually enhance each other. (A)** Representative three-color IF image of VEGFR-2, TSAd and paxillin on the surface of a TIME cell imaged via TIRFM. Red line shows cell edge. Scale bar, 5 µm. **(B–D)** Particle detections (shown as dots in B and C) and patch

segmentation (shown as outlines in D) overlaid on the individual channels for the area within the white box in A. Scale bar, 1 µm. **(E)** Overlay of the three channel detections and segmentations for the area within the black box in B–D, with color coding following that in B–D. Colored circles (diameter = 243 nm) point out the colocalization events between the different molecules, following color-coding in legend at the bottom. Scale bar, 1 µm. **(F)** $-\log_{10}$(P value) table summarizing the significance of each conditional colocalization measure (see text for details) at the indicated colocalization radii, for target = VEGFR-2, reference = FAs and condition = TSAd, in absence and presence of VEGF. Table indicates next to each colocalization measure the molecule subset that it represents. Other details as in Fig. 3 H. **(G and H)** Conditional colocalization measures and their coincidental counterparts ("nullTR" and "randC"; G) and $-\log_{10}$(P value) table summarizing the significance of each conditional colocalization measure (H), at the indicated colocalization radii, for target = TSAd, reference = FAs and condition = VEGFR-2, in absence and presence of VEGF. In G, details as in Fig. 3 G. Only significant conditional colocalization measures, together with $p(TwR)$, are shown. In H, table indicates next to each colocalization measure the molecule subset that it represents. Other details as in Fig. 3 H. **(I and J)** Conditional colocalization measures and their coincidental counterparts (top) and $-\log_{10}$(P value) table summarizing the significance of each conditional colocalization measure (bottom), at the indicated colocalization radii, for target = VEGFR-2, reference = TSAd (I) and vice versa (J), both with condition = FAs, in the absence and presence of VEGF. Only significant conditional colocalization measures, together with $p(TwR)$, are shown in boxplot form. Boxplot figure details as in Fig. 3 G. $-\log_{10}$(P value) table details as in Fig. 3 H. The molecule subsets listed to the left of the tables correspond to the colocalization measures on the far left of I. N = 41 cells from 4 repeats. See Table 3 for number of objects per channel and other dataset properties.

colocalization. First, in terms of colocalization with CCSs, VEGFR-2 and TSAd exhibited (statistical) interdependencies almost the opposite of those observed with FAs; TSAd exhibited overall significant colocalization with CCSs, regardless of its colocalization status with VEGFR-2 (only $p(TwR)$ is significant in Fig. 6 F), while VEGFR-2 colocalization with CCSs was enhanced when it was also colocalized with TSAd ($p(TwR)$ and $p(TwR|TwC)$ are significant in Fig. 6, G and H). Second, in terms of their colocalization with each other, VEGFR-2–TSAd colocalization was significant only for the subset of VEGFR-2 colocalized with CCSs ($p(TwR|TwC)$ in Fig. 6 I and $p^{rs}(Tw(RwC))$ in Fig. 6 J), which was opposite of the case of FAs. Third, while VEGFR-2-TSAd colocalization increased upon stimulation with VEGF (as indicated by more significant P values for a larger range of colocalization radii; Fig. 6, I and J; consistent with observations in context of FAs), TSAd and VEGFR-2 colocalization with CCSs was reduced upon VEGF stimulation (as indicated by overall less significant P values; Fig. 6, F and H). The reduced colocalization with CCSs upon VEGF stimulation suggests that many activated VEGFR-2–TSAd complexes are already internalized after 5 min of stimulation (Lampugnani et al., 2006; Lanahan et al., 2010) and/or CCSs are not the primary mechanism for VEGFR-2 internalization upon stimulation (Basagiannis et al., 2016).

Altogether, these analyses indicate that VEGFR-2-TSAd colocalization varies by location at the plasma membrane. It is enhanced at FAs and CCS. Yet the two membrane domains exhibit differential interplay with VEGFR-2-TSAd colocalization. In the case of FAs, VEGFR-2 and FAs mutually enhance each other's colocalization with TSAd. In the case of CCSs, TSAd and CCSs mutually enhance each other's colocalization with VEGFR-2. To the extent that colocalization is reflective of interactions between VEGFR-2 and TSAd, this raises the question of what leads to this differential interplay of colocalization. One possibility is the presence of different interaction partners or feedback from downstream signaling that modulate these interactions at different membrane domains. Performing further conditional colocalization analysis with other interaction partners and combining it with perturbation of the different molecular players is expected to help determine the molecular mechanisms behind the observed increase in VEGFR-2-TSAd interactions at FAs and CCSs. Importantly, the increased interactions most likely facilitate VEGFR-2 signaling in the right place at the right time to regulate the cellular response to VEGF.

Discussion

We have developed a new approach, conditional colocalization analysis, to assess the colocalization relationships and hierarchies between three molecular entities from multicolor microscopy images. Going beyond the question of whether two entities colocalize, it addresses the question of whether the colocalization between two entities is increased or decreased by a third entity. It exhibits high specificity and sensitivity, especially when integrating analysis results over a range of colocalization radii and complementary conditional colocalization measures. The source code for performing conditional colocalization analysis is available at https://github.com/kjaqaman/conditionalColoc.

Conditional colocalization analysis of multicolor images offers an approach to shed light on the dependencies, hierarchies, and regulation of known molecular interactions within their native, unperturbed environment. It complements the classic approach of system perturbation to probe these questions in at least two ways. First, because it extracts information from the unperturbed system, it can provide unique insights in cases where molecular perturbations have side effects that complicate the interpretation of results, or where there is functional redundancy between molecules (Wagner, 2000; Zhang, 2012). Second, it enables the initial dissection of a system to gather evidence for the important players in regulating the interactions of interest, thus guiding molecular perturbation experiments. Conditional colocalization analysis can be tailored to particular biological questions through question-specific selection of the objects analyzed, e.g., objects from a particular subcellular region or objects of a certain size or shape.

While our applications of conditional colocalization analysis have been focused on the molecular scale, this analytical approach is applicable to any biological system. Non-punctate objects can take any form or shape (Fig. S5), as long as they are relatively discrete and are segmented properly, e.g., using ridge detection for curvilinear objects (Kittisopikul et al., 2020) or using deep learning approaches (Lucas et al., 2021). Punctate objects can be at a relatively high density in the image, in which case their center coordinates can be determined using advanced computer vision approaches designed to handle high-density point emitters (Nehme et al., 2018; Zhu et al., 2012). Accurate detection and/or segmentation of the objects to be analyzed

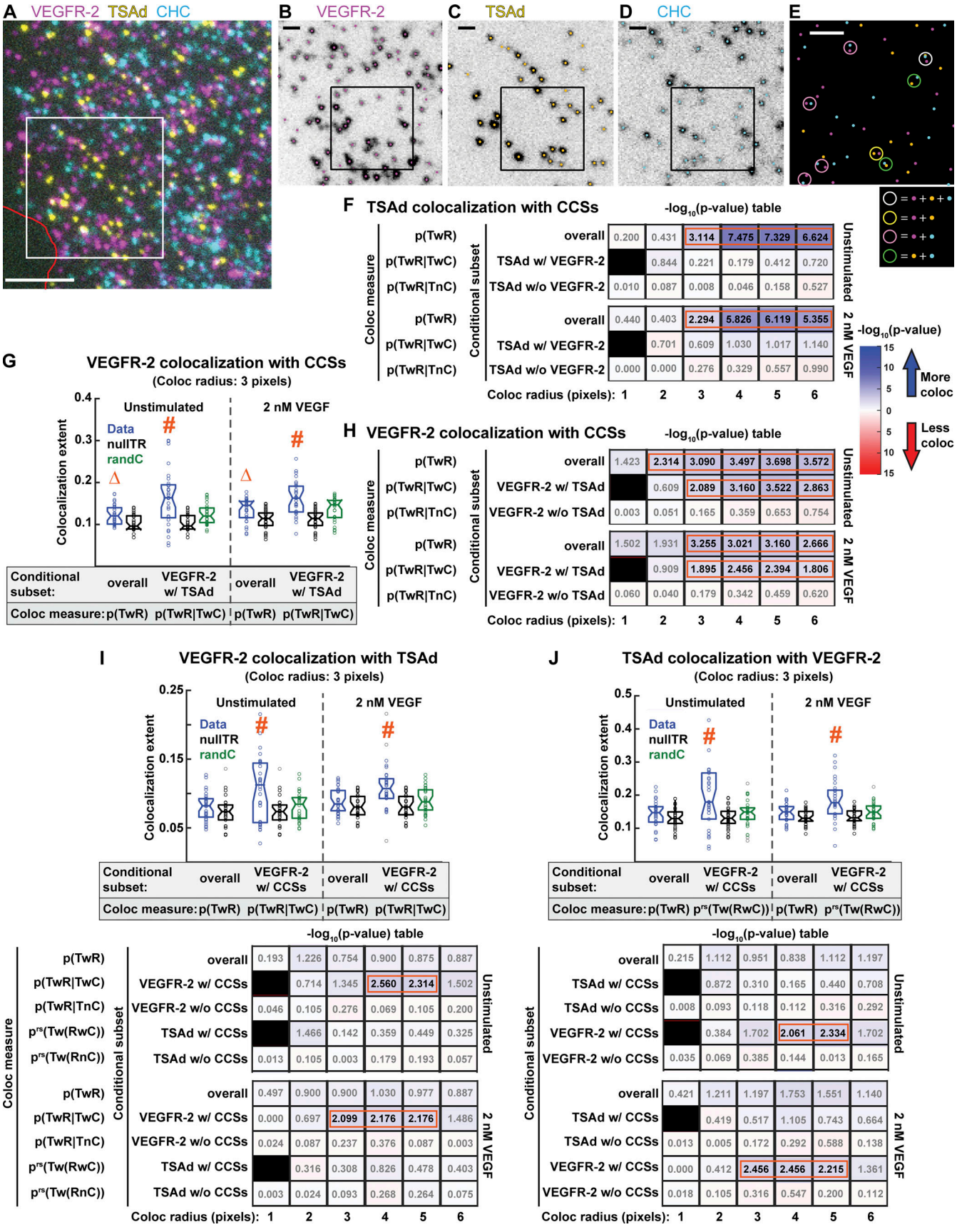

Figure 6. **VEGFR-2-TSAd and VEGFR-2-CCS colocalization mutually enhance each other. (A)** Representative three-color IF image of VEGFR-2, TSAd and CHC on the surface of a TIME cell imaged via TIRFM. Red line shows cell edge. Scale bar, 5 µm. **(B–D)** Particle detections (shown as dots) overlaid on the

individual channels for the area within the white box in A. Scale bar, 1 µm. **(E)** Overlay of the three channel detections for the area within the black box in B–D, with color coding following that in B–D. Colored circles (diameter = 243 nm) point out the colocalization events between the different molecules, following color-coding in legend at the bottom. Scale bar, 1 µm. **(F)** $-\log_{10}$(P value) table summarizing the significance of each conditional colocalization measure (see Text for details) at the indicated colocalization radii, for target = TSAd, reference = CCSs and condition = VEGFR-2, in absence and presence of VEGF. Table indicates next to each colocalization measure the molecule subset that it represents. Other details as in Fig. 3 H. **(G and H)** Conditional colocalization measures and their coincidental counterparts ("nullTR" and "randC"; G) and $-\log_{10}$(P value) table summarizing the significance of each conditional colocalization measure (H), at the indicated colocalization radii, for target = VEGFR-2, reference = CCSs and condition = TSAd, in absence and presence of VEGF. In G, details as in Fig. 3 G, Δ: P < 0.01, indicating that $p(TwR)$ is significantly greater than its coincidental counterpart, as assessed via a Wilcoxon rank-sum test. Only significant conditional colocalization measures, together with $p(TwR)$, are shown. In H, table indicates next to each colocalization measure the molecule subset that it represents. Other details as in Fig. 3 H. **(I and J)** Conditional colocalization measures and their coincidental counterparts (top) and $-\log_{10}$(P value) table summarizing the significance of each conditional colocalization measure (bottom), at the indicated colocalization radii, for target = VEGFR-2, reference = TSAd (I) and vice versa (J), both with condition = CCSs, in the absence and presence of VEGF. Only significant conditional colocalization measures, together with $p(TwR)$, are shown in boxplot form. Boxplot figure details as in Fig. 3 G. $-\log_{10}$(P value) table details as in Fig. 3 H. The molecule subsets listed to the left of the tables correspond to the colocalization measures on the far left of (I). N = 30 cells from 3 repeats. See Table 3 for number of objects per channel and other dataset properties.

increases the accuracy and sensitivity of conditional colocalization analysis.

Furthermore, conditional colocalization analysis can be applied to super-resolution microscopy images, which brings the employed range of colocalization radii closer to molecular dimensions (Huang et al., 2009; Sahl et al., 2017). This will most likely deepen the insight that conditional colocalization analysis provides about molecular interactions and their regulation. Of note, for the application of conditional colocalization analysis to super-resolution data of the localization microscopy type, fluorophore blinking must be corrected for *a priori*, in order to avoid molecule overcounting and artifactual clustering (Hummer et al., 2016; Saguy et al., 2021; Williamson et al., 2020).

Conditional colocalization analysis can be extended in multiple ways. (1) The same analysis can be applied to 2D live-cell images to determine the temporal evolution of colocalization relationships. (2) The analysis can be readily extended to 3D, as long as there is sufficient axial resolution. (3) The analysis can be extended to investigate the colocalization relationships and hierarchies between more than three entities, as long as informative conditional probabilities and related colocalization measures can be defined. As extending the analysis to more than three colors will increase the total number of possible object combinations, the analysis procedure in this case may be iterative to help identify biologically relevant object combinations.

All in all, conditional colocalization analysis is a broadly applicable approach for the analysis of multicolor microscopy images. By quantifying the colocalization relationships between multiple molecular entities, it aids with the dissection of the complex landscape of multimolecular interactions in the cell.

Materials and methods

Cell culture and plating

Human telomerase (hTERT)-immortalized microvascular endothelial cells isolated from human foreskin (TIME cells; ATCC) were grown in ATCC's vascular cell basal medium supplemented with microvascular endothelial cell growth kit-VEGF and 12.5 µg/ml blasticidine (Sigma-Aldrich) for 48 h at 37°C + 5% CO_2 until reaching 80–90% confluence. At confluence, cells were passaged and 5.4 × 10^4 cells were plated on fibronectin-coated (10 µg/ml; MilliporeSigma), base/acid cleaned, 0.17 mm (#1.5) glass-bottom dishes (14 mm glass diameter; MatTek) for 18 h prior to experiments.

Sample preparation for fluorescence imaging

Plated cells were washed once in wash buffer (HBSS + 1 mM HEPES and 0.1% NGS) to remove the culture medium and then incubated with HBSS containing or not 2 nM VEGF-A_{165} (Genscript) for 5 min at 37°C. The incubation solution was then removed and cells were fixed with a 3.2% paraformaldehyde solution made in PBS (Electron Microscopy Sciences) for 15 min at RT. Samples were then washed three times (5 min each) at RT with wash buffer and then permeabilized for 1 min with cold 0.01% Triton X-100 solution made in PBS. After three washes, samples were blocked for 15 min in blocking buffer (1% BSA, 5% NGS in wash buffer) and then incubated for 1 hr with primary antibodies (Table 1) at RT. After three washes, samples were incubated with secondary antibodies (Table 1) for 15 min at RT. After three more washes, they were incubated with AlexaFluor647-conjugated primary antibodies (Table 1) for 15 min at RT. Finally, after three subsequent washes, dishes were incubated with imaging buffer (Oxyfluor 1%, Glucose 0.45%, Trolox 2 nM) to reduce photobleaching.

Total internal reflection fluorescence microscopy (TIRFM)

Cells were imaged at 37°C using an Olympus IX83 TIRF microscope equipped with a Z-Drift Compensator and a UAPO 100X/1.49 NA oil-immersion TIRF objective (Olympus). The microscope was equipped with an iXon 888 1k × 1k EMCCD Camera (Andor; Oxford Instruments). With an additional 1.6× magnification in place, the pixel size in the recorded image was 81 nm × 81 nm. Using the Olympus CellSens software, excitation light of 640, 561, and 491 nm from an Olympus CellTIRF-4Line laser system was directed to the sample at a penetration depth of 90 nm by a TRF8001-OL3 Quad-band dichroic mirror. Fluorescence of different wavelengths was collected, filtered with emission filters of ET520/40m, ET605/52m, and ET705/72m (Chroma), and projected onto different sections of the camera chip by an OptoSplit III 3-channel image splitter (Cairn Research). The different channels were excited and recorded sequentially in the order 640, then 561, and then 491. Images were acquired with MetaMorph (Molecular Devices). Camera EM gain was set to 100 for all acquisitions.

Table 1. **Primary and secondary antibodies and their dilutions used for IF imaging**

Antibody	Host, clonality	Manufacturer (identifier)	Dilution used
Unconjugated primary			
Anti TfR	Rabbit, polyclonal	Abcam, ab84036	1:200
Anti TSAd (OTI4F3)	Mouse, monoclonal	Invitrogen, MA5-25894	1:100
Anti activated β1-integrin (P4G11)	Mouse, monoclonal	Sigma-Aldrich, MAB1951	1:10,000
Anti pFAK (pY397) (EP2160Y)	Rabbit, monoclonal	Abcam, ab81298	1:10,000
Anti VEGFR-2 (55B11)	Rabbit, monoclonal	Cell Signaling Technology, #2479	1:400
Conjugated primary			
Alexa Fluor 647 Anti-Paxillin (Y113)	Rabbit, monoclonal	Abcam, ab246719	1:100
Alexa Fluor 647 Anti-CHC (X22)	Mouse, monoclonal	Invitrogen, MA1-065-A647	1:2,000
Secondary			
Alexa Fluor 488 Anti-Mouse IgG secondary	Goat, polyclonal	Invitrogen, A-11029	1:1,000
Alexa Fluor 546 Anti-Rabbit IgG secondary	Goat, polyclonal	Invitrogen, A-11010	1:1,000
Alexa Fluor 488 Anti-Rabbit IgG secondary	Goat, polyclonal	Invitrogen, A-11008	1:10,000
Alexa Fluor 546 Anti-Mouse IgG secondary	Goat, polyclonal	Invitrogen, A-11003	1:10,000

For all datasets, except for activated β_1-integrin/pFAK/paxillin, each channel was imaged once using an exposure time of 99 ms and a power of 3.6, 6.4, and 5.9 mW at the coverslip (measured with a Thorlabs power meter at an incident angle of 0°) for the 491, 561, and 640 nm lasers, respectively. For the activated β_1-integrin/pFAK/paxillin combination, two types of images were collected, before and after photobleaching. Specifically, β_1-integrin and pFAK were imaged in a streaming mode for 300 frames (at 10 Hz) with laser power increased to 5.4 mW for the 491 channel and 9.6 mW for the 561 channel to photobleach the signal. The first frame of each stream, where the β_1-integrin and pFAK signals were largely non-punctate, was used for conditional colocalization analysis of all non-punctate objects (Fig. S5). To also obtain punctate images for β_1-integrin and pFAK, a single image was acquired for each of them after photobleaching, and this was used for colocalization analysis of punctate target and reference objects together with non-punctate condition objects (Figs. 3 and 4). Paxillin (the 640 channel) was imaged only once, as with the other molecule combinations.

For every three-channel image or movie, a brightfield snapshot of the imaged cell region was also acquired, in order to aid with manual delineation of the region of interest (ROI) mask for the ensuing analysis.

Computing environment

All image and data analysis and simulation tasks were performed in Matlab R2020a (The MathWorks). All employed code and software packages are compatible with Matlab R2020a on a Linux 64-bit operating system. Images were loaded into Matlab using Bio-Formats (Linkert et al., 2010).

Punctate object detection

Punctate objects were detected using the "point-source detection" particle detection algorithm in u-track (https://github.com/DanuserLab/u-track; Aguet et al., 2013; Jaqaman et al., 2008). In brief, the algorithm consists of two steps: (i) a filtering step to determine pixels likely to contain objects and (ii) a Gaussian fitting step to determine the object positions with subpixel localization. With the appropriate, wavelength-dependent standard deviation, a two-dimensional Gaussian is a good approximation of the microscope's point spread function (Thomann et al., 2002; Zhang et al., 2007). Largely default parameter values were used, except for the α-value for determining object detection significance by comparing the fitted Gaussian amplitude to the local background noise distribution (Table 2). The α-value was chosen based on the visual assessment of the detection results with the goal of minimizing both false positives (superfluous detections) and false negatives (missed particles). The number of objects detected within the ROI for each dataset is listed in Table 3.

Non-punctate object segmentation

Non-punctate objects were segmented using an intensity threshold to separate foreground from the background (Jaqaman et al., 2016). The threshold was determined for each image individually. For paxillin, it was taken as the 90th percentile of each image's intensity distribution after noise filtering (using a Gaussian kernel with standard deviation = 1 pixel) and local background subtraction. For β_1-integrin and pFAK (when the non-punctate version of their images was analyzed), the threshold was taken as the 85th percentile, also after the above-described pre-processing steps. The local background was estimated for each image by filtering it with a Gaussian kernel with standard deviation = 10 pixels. The threshold was then applied to the noise-filtered and background-subtracted image to segment the patches. Patches with an area of at least 30 pixels (in the case of paxillin and pFAK) or 10 pixels (in the case of β_1-integrin) were retained for further analysis. The number of segmented patches within the ROI and their areas are listed in Tables 3 and 4. The slight differences in paxillin segmentation properties for the β_1-Integrin/pFAK/paxillin dataset between the two tables

Table 2. **Three-channel imaging and detection of indicated molecule combinations**

	Channel wavelength	PSF sigma (pixels, nm)	Parameters
TfR/TSAd/CHC			
TfR	561	1.4, 113	Alpha: 0.01, all others: default
TSAd	488	1.2, 97	Alpha: 0.01, all others: default
CHC	640	1.58, 128	Alpha: 0.05, all others: default
Activated β_1-integrin/pFAK/paxillin			
Activated β_1-integrin	561	1.4, 113	Alpha: 0.01, all others: default
pFAK	488	1.2, 97	Alpha: 0.01, all others: default
Paxillin	640	N/A	N/A
VEGFR-2/TSAd/CHC			
VEGFR-2	561	1.4, 113	Alpha: 0.05, all others: default
TSAd	488	1.2, 97	Alpha: 0.01, all others: default
CHC	640	1.58, 128	Alpha: 0.05, all others: default
VEGFR-2/TSAd/paxillin			
VEGFR-2	561	1.4, 113	Alpha: 0.05, all others: default
TSAd	488	1.2, 97	Alpha: 0.01, all others: default
Paxillin	640	N/A	N/A

PSF, point spread function. Shown are the parameters of the "point-source detection" particle detection algorithm in u-track that vary between channels and datasets. Two other parameters that change (namely "Max Fit Adjust" and "Fit Window Size") are not shown because they were given their default values of 2 × PSF sigma and 4 × PSF sigma, respectively. The paxillin channel has N/A parameters because it was not detected using point-source detection due to its non-punctate nature.

are because of the slightly different ROIs employed for analysis when all channels of this dataset were non-punctate (Table 4) vs. when only the paxillin channel was non-punctate (Table 3).

Region of interest (ROI) mask segmentation

ROI masks, covering the imaged area of each cell of interest, were delineated manually. For TfR/TSAd/CHC and VEGFR-2/TSAd/CHC, delineation was based on the brightfield image. For VEGFR-2/TSAd/paxillin and β_1-integrin/pFAK/paxillin, delineation was based on the brightfield image as well as the paxillin and pFAK images (where acquired).

Core algorithm to calculate a fraction of target colocalized with reference

Our implementation closely followed the original algorithm proposed in Helmuth et al., (2010). A target object was considered to be colocalized with a reference object if the colocalization distance between it and its nearest neighbor reference object (see Results section "Generalization of conditional colocalization analysis to non-punctate objects" for colocalization distance definition) was smaller than a user-defined threshold ("colocalization radius"). The colocalization radius accounted for various considerations, such as registration shifts between channels, segmentation accuracy, average object size, etc. For a given subset of target objects, the fraction of target colocalized with reference (f_{coloc}) was then calculated as the ratio of the number of target objects colocalized with reference objects to the total number of target objects in that subset.

To calculate the coincidental colocalization fraction of the target with the reference (f_{coloc}^{nullTR}) given the cellular context, in particular the number, spatial distribution, size, and shape of reference objects within the ROI mask, in the case of punctate target objects, we followed Helmuth et al. (2010) and replaced the target positions with a grid of positions covering the whole ROI. Specifically, we used each pixel within the ROI as one grid point (i.e., target position), and repeated the above distance calculations, classification, and fraction calculation. In the case of non-punctate target objects, using a grid was no longer applicable because it would not preserve the nature (i.e., general size and shape) of target objects. Therefore, instead of a grid, in this case, we randomized the target object positions within the ROI mask (see next section for details) and repeated the above distance calculations, classification, and fraction calculation. This was performed 100 times to minimize fluctuations (Fig. S1 H).

Position randomization of condition or target objects within the ROI mask

Objects were randomized within the ROI mask for two purposes. (1) To calculate the conditional colocalization probabilities expected by chance, i.e., in the absence of any true influence of the condition objects on target-reference colocalization, the condition objects (whether punctate or non-punctate) were randomized within the ROI mask. (2) To calculate the coincidental colocalization fraction of target with reference in the case of non-punctate target, the target objects were randomized within the cell mask (as mentioned above). For both cases, randomization was performed 100 times to minimize fluctuations (Fig. S1, G and H).

For randomizing punctate condition objects, to ensure that none of the randomly chosen locations were too close to the ROI mask boundary, the ROI mask was first eroded using a square structuring element with a size equal to the colocalization radius plus three pixels. The new condition object locations were then chosen within the eroded ROI mask, using the same number of condition objects as in the original data.

For randomizing non-punctate condition objects or non-punctate target objects, we conserved not only the number of objects, but also the shape of each object. To optimize the selection of random locations, objects in this case were placed in random locations sequentially, starting with the largest object and going down to the smallest object. The idea behind this order was that it was easier to place small objects between large

Table 3. **Number of objects per ROI, ROI area, and segmented patch area (where applicable) for the various experimental datasets**

Dataset (channels 1/2/3, i.e., 561/488/640)	Channel 1 objects per ROI [min max] avg	Channel 2 objects per ROI [min max] avg	Channel 3 objects per ROI [min max] avg	ROI area (pixels²) [min max] avg	Segmented patch area (pixels²) [min max] avg
TfR/TSAd/CHC	[151 660] 368	[80 506] 214	[233 751] 490	[85,190 219,960] 156,800	N/A
β_1-Integrin/pFAK/paxillin	[157 804] 371	[424 1,561] 910	[47 178] 101	[61,570 234,760] 132,950	[31 1,819] 113
VEGFR-2/TSAd/paxillin	[357 1,194] 754	[174 663] 358	[46 225] 134	[93,880 231,610] 158,340	[31 1,655] 96
VEGFR-2/TSAd/CHC	[352 1,134] 695	[200 639] 415	[284 928] 568	[62,510 202,080] 144,870	N/A

objects than the other way around. Once an object was placed, the pixels it occupied were removed from the ROI mask, as those pixels were no longer available for any other object (Fig. S1, A–F). In addition, before placing each object, the mask was eroded using a disk-structing element with a radius equal to the average radius of the object being placed (Fig. S1, A–F). The purpose of this was to avoid placing any new object too close to already-placed objects (leading to overlap) or to the ROI mask boundary (leading to part of the object being outside the ROI mask). With this strategy, we were able to randomize the locations of non-punctate objects within the ROI mask while avoiding any overlap between them and while avoiding the scenario of not enough contiguous space to place larger objects (a scenario that happened often when smaller objects were placed before larger objects).

Validation simulations: Overview

The validation simulations were performed within cell ROI masks taken from our experimental data to keep the simulations as realistic as possible. Several masks were used as repeats for each parameter combination, as described in Results. Cell masks were eroded using a square element with side length = 10 pixels to avoid molecules being positioned too close to the cell edge. Below, we list the parameter combinations employed for validation testing and the simulation strategies for the various scenarios.

Validation simulations: Parameter combinations

Two sets of objects

(i) Punctate target and reference. N_T = 150, 200, 250, 300, 350, N_R = 150, 200, 250, 300, 350 and $p(TwR)$ = 0, 0.25, 0.5, 0.75, 1. Total: 125 parameter combinations. (ii) Punctate target and non-punctate reference. N_T = 150, 200, 250, 300, 350 and $p(TwR)$ = 0, 0.25, 0.5, 0.75, 1. Reference objects were taken from our experimental data paxillin patch segmentations. Total: 25 parameter combinations. (iii) Non-punctate target and reference. Reference objects were taken from our experimental data paxillin patch segmentations and combined with ellipsoidal target objects that mimicked paxillin patches (Fig. S3, A–C). N_T = 85 (lower than the N_T employed above to accommodate the larger size of non-punctate target objects) and $p(TwR)$ = 0, 0.25, 0.5, 0.75, 1. Total: 5 parameter combinations.

Table 4. **Number of segmented objects, the segmented patch area, and ROI area for the β_1-integrin/pFAK/paxillin dataset when analyzed as all non-punctate objects**

Property	Channel 1 [min max] avg	Channel 2 [min max] avg	Channel 3 [min max] avg
Objects per ROI	[123 520] 279	[95 359] 214	[47 184] 107
Segmented patch area (pixels²)	[11 1,575] 74	[31 1,183] 77	[31 1,811] 113
ROI area (pixels²)	[61,390 242,330] 141,190		

Three sets of objects

(i) Punctate target, reference, and condition. Given the observation that the estimated $p(TwR)$ was equally accurate for all tested N_T and N_R (Fig. 2, A and B), N_T and N_R were fixed at 250 (middle of the range tested for two sets of objects). Otherwise, N_C = 250, 300 and 350, $p(TwC)$ = 0.25, 0.5, 0.75, $p(RwC)$ = 0.25, 0.5, 0.75, $p(TwR|TwC)$ = 0.25, 0.5, 0.75, and $p(TwR|TnC)$ = 0.25, 0.5, 0.75. Total: 243 parameter combinations. (ii) Punctate target and reference, and non-punctate condition. N_T and N_R were fixed at 250. Condition objects were taken from our experimental data paxillin patch segmentations. $p(TwC)$ = 0.25, 0.5, 0.75, $p(RwC)$ = 0.25, 0.5, 0.75, $p(TwR|TwC)$ = 0.25, 0.5, 0.75 and $p(TwR|TnC)$ = 0.25, 0.5, 0.75. Total: 81 parameter combinations. (iii) Non-punctate target, reference, and condition. Condition objects were taken from our experimental data paxillin patch segmentations and combined with N_T = 85 non-punctate, ellipsoidal target objects and N_R = 90 non-punctate, ellipsoidal reference objects (Fig. S3, A and B). $p(TwC)$ = 0.25, $p(RwC)$ = 0.25, and two combinations of $p(TwR|TwC)$ and $p(TwR|TnC)$, namely 0.75 and 0.25 and the reverse. Total: 2 parameter combinations.

Validation simulations: Simulation strategy

Two sets of objects

(i) Punctate target and non-punctate reference. To simulate non-punctate reference objects, the paxillin patch segmentations belonging to the employed cell masks were used as reference objects. Then, based on the input $p(TwR)$, target objects were divided into colocalized or not colocalized with reference objects. Target objects colocalized with reference objects were placed 0–2 pixels from the boundaries of the reference objects with which they were associated. Target objects not colocalized

with reference objects were placed at random coordinates within the eroded cell mask, excluding the pixels belonging to reference objects. For this, the reference objects were dilated using a square element with side length = 10 pixels to exclude the colocalization area around each reference object when placing not-colocalized target objects.

(ii) Punctate target and reference. These simulations followed the strategy described in Point i. The only difference was that they did not use the experimental paxillin patch segmentations for reference objects. Instead, reference objects were placed at random coordinates within the eroded cell mask, and a binary image was created where pixels of value one represented the positions of reference objects. These masks were the starting point for the simulations, as described for the previous case.

(iii) Non-punctate target and reference. These simulations also followed the strategy described in Point i. The only difference was that non-punctate target objects were generated by dilating their center points, which were placed near or not near reference objects as in Point i, first with a line of length 7 pixels and a random orientation between 0 and 180° and then with a disk of radius 5 pixels. This generated ellipsoidal target objects with an area of 123 pixels^2 and eccentricity of 0.79, which were within the range of object size and eccentricity observed for paxillin patches (Fig. S3, A–C).

Three sets of objects

(i) Punctate target and reference and non-punctate condition. As with the case above of non-punctate reference objects, the paxillin patch segmentations belonging to the employed cell masks were used for the simulations, but this time as condition objects. Based on the input $p(TwC)$ and $p(RwC)$, target and reference objects, were divided into condition-positive and condition-negative groups. Condition-positive reference objects were placed 0.2 pixels away from the boundaries of the condition objects with which they were associated. This very close placement was motivated by practical considerations, making it easier to place target objects (as described next) close to both a reference object and a condition object when needed, as being placed close to one almost guaranteed being placed close to the other. Condition-negative reference objects were placed at random coordinates within the eroded cell mask, excluding the pixels belonging to condition objects after dilating them using a square element with side length = 10 pixels.

To place target objects, they were subdivided further. First, based on $p(TwR|TwC)$, the condition-positive target objects were divided into colocalized or not colocalized with reference objects. Condition-positive target objects colocalized with reference objects were placed 0–2 pixels from condition-positive reference objects. Given the placement scheme for condition-positive reference objects, this almost guaranteed that the target objects were colocalized with condition objects as well. Condition-positive target objects not colocalized with reference objects were placed 0–2 pixels from the boundaries of condition objects, after eliminating the boundary pixels associated with reference objects. Second, based on $p(TwR|TnC)$, condition-negative target objects were divided into colocalized or not with reference objects. Condition-negative target objects colocalized with reference objects were placed 0–2 pixels from condition-negative reference objects, which largely placed them far from condition objects as well. Condition-negative target objects not colocalized with reference objects were placed at random coordinates within the eroded cell mask, excluding the pixels belonging to condition objects and reference objects, both after dilation using a square element with side length = 10 pixels.

(ii) Punctate target, reference, and condition. These simulations followed the strategy described in Point i. The only difference was that they did not use the experimental paxillin patch segmentations for condition objects. Instead, condition objects were placed at random coordinates within the eroded cell mask and a binary image was created where pixels of value one represented the positions of condition objects. These masks were the starting point for the simulations as described in the previous case.

(iii) Non-punctate target, reference, and condition. These simulations also followed the strategy described in Point i. The only difference was that non-punctate target and reference objects were generated by dilating their center points, which were placed near or not near condition objects and/or each other as in Point i, first with a line of length 7 pixels and a random orientation between 0 and 180° and then with a disk of radius 3 pixels for target objects or of radius 5 pixels for reference objects. This generated ellipsoidal target objects with an area of 55 pixels^2 and an eccentricity of 0.79 and ellipsoidal reference objects with an area of 123 pixels^2 and eccentricity of 0.79, which were within the range of object size and eccentricity observed for paxillin patches (Fig. S3, A and B).

The conditional colocalization measures in the context of the joint probability distribution

As mentioned in Results, the conditional colocalization measures employed in this work are conceptually related to the joint probability distribution describing the colocalization of target, reference, and condition. They explore different facets of the joint probability distribution in order to directly address the question of how much the condition influences the extent of target colocalization with reference.

Here we describe a mapping between our conditional colocalization measures and the joint probability distribution. Specifically, suppose that the joint probability distribution for the colocalization of target, reference and condition is given by $q(TRC)$. In this formulation, an object is a "compound object" defined across all three channels, where T = 0/1, R = 0/1, and C = 0/1, indicating that the compound object contains/does not contain a target, reference, and a condition object, respectively. Note that, in order to define compound objects that contain a maximum of one of each object type (T, R, and C), the radius employed for defining compound objects (akin to the colocalization radius employed in our analysis) must be smaller than the minimum inter-object distance within each channel. This puts an upper limit on the radius, which may limit the ability to construct the joint probability distribution in practice, depending on the nature of the analyzed images. Nevertheless, on a conceptual level, there is a mapping between our conditional colocalization measures and the joint probability distribution.

For the below equations, it is convenient to define two marginal distributions derived from the joint probability distribution. First, the probability of a compound object to contain a target object regardless of the presence of reference or condition objects, $Q(T = 1)$:

$$Q(T = 1) = q(111) + q(101) + q(110) + q(100). \quad (12)$$

Second, the probability of a compound object to contain a reference object regardless of the presence of target or condition objects, $Q(R = 1)$:

$$Q(R = 1) = q(111) + q(011) + q(110) + q(010). \quad (13)$$

Using this nomenclature, the conditional colocalization measures are related to the joint probability distribution as follows. Eq. 1:

$$p(TwC) = \frac{q(111) + q(101)}{Q(T = 1)}. \quad (14)$$

Complementing Eq. 14,

$$p(TnC) = \frac{q(110) + q(100)}{Q(T = 1)}. \quad (15)$$

Eq. 2:

$$p(RwC) = \frac{q(111) + q(011)}{Q(R = 1)}. \quad (16)$$

Complementing Eq. 16,

$$p(RnC) = \frac{q(110) + q(010)}{Q(R = 1)}. \quad (17)$$

Eq. 3:

$$p(TwR) = \frac{q(111) + q(110)}{Q(T = 1)}. \quad (18)$$

Eq. 6:

$$p(TwR|TwC) = \frac{q(111)}{q(111) + q(101)}. \quad (19)$$

Eq. 7:

$$p(TwR|TnC) = \frac{q(110)}{q(110) + q(100)}. \quad (20)$$

Eq. 10:

$$p^{rs}(Tw(RwC)) = p(Tw(RwC))/p(RwC)$$
$$= \frac{q(111)}{Q(T = 1)} \Big/ \frac{q(111) + q(011)}{Q(R = 1)} = \left(\frac{q(111)}{q(111) + q(011)}\right) \frac{Q(R = 1)}{Q(T = 1)}. \quad (21)$$

Eq. 11:

$$p^{rs}(Tw(RnC)) = p(Tw(RnC))/p(RnC)$$
$$= \frac{q(110)}{Q(T = 1)} \Big/ \frac{q(110) + q(010)}{Q(R = 1)} = \left(\frac{q(110)}{q(110) + q(010)}\right) \frac{Q(R = 1)}{Q(T = 1)}. \quad (22)$$

Derivation of expected colocalization measures from simulation input parameters

In our simulations, $p(TwC)$, $p(RwC)$, $p(TwR|TwC)$, and $p(TwR|TnC)$ were explicitly defined as input parameters. For the validation of our conditional colocalization analysis, their calculated values were compared directly to their input values. The remaining two conditional colocalization measures, $p^{rs}(Tw(RwC))$ and $p^{rs}(Tw(RnC))$, and the overall colocalization probability $p(TwR)$, were not explicitly defined. Thus, for validation, their calculated values were compared to their expected values, which were derived from the input $p(TwC)$, $p(RwC)$, $p(TwR|TwC)$ and $p(TwR|TnC)$ and Eqs. 12, 13, 14, 15, 16, 17, 18, 19, 20, 21, and 22 above.

$p(TwR)$:

$$p(TwR) = \frac{q(111) + q(101)}{Q(T = 1)} = \frac{q(111)}{Q(T = 1)} + \frac{q(101)}{Q(T = 1)}$$

(Eq. 18)

$$= \left(\frac{q(111)}{q(111) + q(101)}\right)\left(\frac{q(111) + q(101)}{Q(T = 1)}\right) + \left(\frac{q(110)}{q(110) + q(100)}\right) \times \left(\frac{q(110) + q(100)}{Q(T = 1)}\right)$$

(arithmetic manipulation)

$$= p(TwR|TwC)p(TwC) + p(TwR|TnC)p(TnC)$$

(Eqs. 14, 15, 19, and 20)

$$= p(TwR|TwC)p(TwC) + p(TwR|TnC)(1 - p(TwC)). \quad (23)$$

Eq. 23 reflects the law of total probability relating $p(TwR)$ to the conditional probabilities $p(TwR|TwC)$ and $p(TwR|TnC)$.

$p^{rs}(Tw(RwC))$:

$$p^{rs}(Tw(RwC)) = \left(\frac{q(111)}{q(111) + q(011)}\right) \frac{Q(R = 1)}{Q(T = 1)}$$

(Eq. 21)

$$= \left(\frac{q(111)}{q(111) + q(101)}\right)\left(\frac{q(111) + q(101)}{q(111) + q(011)}\right) \frac{Q(R = 1)}{Q(T = 1)}$$

(arithmetic manipulation)

$$= \left(\frac{q(111)}{q(111) + q(101)}\right)\left(\frac{q(111) + q(101)}{Q(T = 1)}\right)\left(\frac{Q(R = 1)}{q(111) + q(011)}\right)$$

(arithmetic manipulation)

$$= p(TwR|TwC)p(TwC)/p(RwC) \quad (24)$$

(Eqs. 14, 16, and 19).

$p^{rs}(Tw(RnC))$:

$$p^{rs}(Tw(RnC)) = \left(\frac{q(110)}{q(110) + q(010)}\right) \frac{Q(R = 1)}{Q(T = 1)}$$

(Eq. 22)

$$= \left(\frac{q(110)}{q(110) + q(100)}\right)\left(\frac{q(110) + q(100)}{q(110) + q(010)}\right) \frac{Q(R = 1)}{Q(T = 1)}$$

(arithmetic manipulation)

$$= \left(\frac{q(110)}{q(110) + q(100)}\right)\left(\frac{q(110) + q(100)}{Q(T = 1)}\right)\left(\frac{Q(R = 1)}{q(110) + q(010)}\right)$$

(arithmetic manipulation)

$$= p(TwR|TnC)p(TnC)/p(RnC) \quad (25)$$

(Eqs. 15, 17, and 20).

Signal-to-noise ratio (SNR) estimation and addition of noise to reduce image SNR

The SNR of an image was defined as:

$$SNR = \frac{I_{obj} - \mu_{Bkg}}{\sigma_{Bkg}},$$

where I_{obj} was the mean intensity of all objects detected in the image, μ_{Bkg} was the background intensity mean and σ_{Bkg} was the background intensity standard deviation. Object intensity was taken as the intensity at the center position for punctate objects or as the average intensity over all pixels belonging to an object for non-punctate objects. To calculate the mean and standard deviation of background intensity, background pixels in the image were defined as follows: In the case of punctate objects, background pixels were taken as all pixels within the ROI mask but not within a 4-pixel radius from the center coordinates of detected objects. In the case of non-punctate objects, background pixels were taken as all pixels within the ROI mask but not within 2 pixels from the boundaries of segmented objects.

To reduce image SNR from its original value to 4, 3, and 2 (Fig. 4), Gaussian white noise was added to the images. The standard deviation of the added noise was adjusted to reach the desired SNR as follows:

Suppose an image has an original SNR of S_0, and thus an original background intensity standard deviation of:

$$\sigma_{Bkg,0} = \frac{I_{obj} - \mu_{Bkg}}{S_0}.$$

To reduce the SNR of this image to some desired SNR S_T, its background intensity standard deviation must be increased to:

$$\sigma_{Bkg,T} = \frac{I_{obj} - \mu_{Bkg}}{S_T}.$$

As the added noise is Gaussian, and assuming that the image noise is Gaussian, it follows that the added noise must have a standard deviation of:

$$\sigma_{add} = \sqrt{\sigma^2_{Bkg,T} - \sigma^2_{Bkg,0}}.$$

If the introduction of additional noise rendered some intensity values negative, the mean background intensity was increased to ensure that all intensity values remained positive after the added noise.

Online supplemental material

Fig. S1 shows example illustrating the randomization procedure for non-punctate objects and convergence of calculated coincidental measures upon randomization. Fig. S2 Illustrates the colocalization distance for two general, non-punctate objects and its dependence on their relative location, size and shape. Fig. S3 shows properties of segmented paxillin patches and further colocalization analysis of simulated non-punctate objects. Fig. S4 shows the results of applying conditional colocalization analysis to an experimental negative control. Fig. S5 shows the results of applying conditional colocalization analysis to non-punctate images of activated β_1-integrin, pFAK and paxillin.

Acknowledgments

We thank Dr. Tieqiao Zhang for microscopy support, Dr. Anthony R. Vega for initial programming of code for pairwise colocalization of punctate objects, and Dr. Nicolas Touret (University of Alberta, Edmonton) for critical reading of the manuscript.

This work was supported by funding from National Institutes of Health/National Institute of General Medical Sciences (R35 GM119619), the Welch Foundation (I-1901), the National Science Foundation (MCB-2114417), and the University of Texas Southwestern Endowed Scholars Program to K. Jaqaman. J. Vega-Lugo was an honorary trainee of the National Institutes of Health Molecular Biophysics Training Grant (5T32GM131963; PI: Dr. Yuh Min Chook) and was also supported by a Diversity Supplement to National Institutes of Health grant R35 GM119619 (PI: K. Jaqaman).

The authors declare no competing financial interests.

Author contributions: K. Jaqaman, J. Vega-Lugo and B. Rocha-Azevedo designed research; J. Vega-Lugo and K. Jaqaman developed algorithm; J. Vega-Lugo wrote software; B. Rocha-Azevedo and A. Dasgupta performed experiments; J. Vega-Lugo and B. Rocha-Azevedo performed analysis; K. Jaqaman, J. Vega-Lugo and B. Rocha-Azevedo wrote paper with input from A. Dasgupta.

Submitted: 21 June 2021
Revised: 15 March 2022
Accepted: 25 April 2022

References

Aaron, J.S., A.B. Taylor, and T.L. Chew. 2018. Image co-localization: Co-occurrence versus correlation. *J. Cell Science.* 131:jcs211847. https://doi.org/10.1242/jcs.211847

Abedi, H., and I. Zachary. 1997. Vascular endothelial growth factor stimulates tyrosine phosphorylation and recruitment to new focal adhesions of focal adhesion kinase and paxillin in endothelial cells. *J. Biol. Chem.* 272: 15442–15451. https://doi.org/10.1074/jbc.272.24.15442

Adler, J., S.N. Pagakis, and I. Parmryd. 2008. Replicate-based noise corrected correlation for accurate measurements of colocalization. *J. Microsc.* 230: 121–133. https://doi.org/10.1111/j.1365-2818.2008.01967.x

Aguet, F., C.N. Antonescu, M. Mettlen, S.L. Schmid, and G. Danuser. 2013. Advances in analysis of low signal-to-noise images link dynamin and AP_2 to the functions of an endocytic checkpoint. *Dev. Cell.* 26:279–291. https://doi.org/10.1016/j.devcel.2013.06.019

Andronov, L., I. Orlov, Y. Lutz, J.L. Vonesch, and B.P. Klaholz. 2016. ClusterViSu, a method for clustering of protein complexes by Voronoi tessellation in super-resolution microscopy. *Sci. Rep.* 6:24084. https://doi.org/10.1038/srep24084

Basagiannis, D., S. Zografou, C. Murphy, T. Fotsis, L. Morbidelli, M. Ziche, C. Bleck, J. Mercer, and S. Christoforidis. 2016. VEGF induces signalling and angiogenesis by directing $VEGFR_2$ internalisation through macropinocytosis. *J. Cell Sci.* 129:4091–4104. https://doi.org/10.1242/jcs.188219

Bates, M., B. Huang, G.T. Dempsey, and X. Zhuang. 2007. Multicolor super-resolution imaging with photo-switchable fluorescent probes. *Science.* 317:1749–1753. https://doi.org/10.1126/science.1146598

Birch, C.A., O. Molinar-Inglis, and J. Trejo. 2021. Subcellular hot spots of GPCR signaling promote vascular inflammation. *Curr. Opin. Endocr. Metab. Res.* 16:37–42. https://doi.org/10.1016/j.coemr.2020.07.011

Birukova, A.A., I. Cokic, N. Moldobaeva, and K.G. Birukov. 2009. Paxillin is involved in the differential regulation of endothelial barrier by HGF and

VEGF. *Am. J. Respir. Cell Mol. Biol.* 40:99–107. https://doi.org/10.1165/rcmb.2008-0099OC

Bolte, S., and F.P. Cordelières. 2006. A guided tour into subcellular colocalization analysis in light microscopy. *J. Microsc.* 224:213–232. https://doi.org/10.1111/j.1365-2818.2006.01706.x

Boutte, Y., M.T. Crosnier, N. Carraro, J. Traas, and B. Satiat-Jeunemaitre. 2006. The plasma membrane recycling pathway and cell polarity in plants: Studies on PIN proteins. *J. Cell Sci.* 119:1255–1265. https://doi.org/10.1242/jcs.02847

Caetano, F.A., B.S. Dirk, J.H.K. Tam, P.C. Cavanagh, M. Goiko, S.S.G. Ferguson, S.H. Pasternak, J.D. Dikeakos, J.R. de Bruyn, and B. Heit. 2015. MIiSR: Molecular interactions in super-resolution imaging enables the analysis of protein interactions, dynamics and formation of multiprotein structures. *PLoS Comput. Biol.* 11:e1004634. https://doi.org/10.1371/journal.pcbi.1004634

Costes, S.V., D. Daelemans, E.H. Cho, Z. Dobbin, G. Pavlakis, and S. Lockett. 2004. Automatic and quantitative measurement of protein-protein colocalization in live cells. *Biophys. J.* 86:3993–4003. https://doi.org/10.1529/biophysj.103.038422

da Rocha-Azevedo, B., S. Lee, A. Dasgupta, A.R. Vega, L.R. de Oliveira, T. Kim, M. Kittisopikul, Z.A. Malik, and K. Jaqaman. 2020. Heterogeneity in VEGF receptor-2 mobility and organization on the endothelial cell surface leads to diverse models of activation by VEGF. *Cell Rep.* 32:108187. https://doi.org/10.1016/j.celrep.2020.108187

Delos Santos, R.C., C. Garay, and C.N. Antonescu. 2015. Charming neighborhoods on the cell surface: Plasma membrane microdomains regulate receptor tyrosine kinase signaling. *Cell. Signal.* 27:1963–1976. https://doi.org/10.1016/j.cellsig.2015.07.004

Diggle, P.J. 2014. Statistical Analysis of Spatial and Spatiotemporal Point Patterns. CRC Press, Boca Raton, FL.

Dunn, K.W., M.M. Kamocka, and J.H. McDonald. 2011. A practical guide to evaluating colocalization in biological microscopy. *Am. J. Physiol. Cell Physiol.* 300:C723–C742. https://doi.org/10.1152/ajpcell.00462.2010

Eichmann, A., and M. Simons. 2012. VEGF signaling inside vascular endothelial cells and beyond. *Curr. Opin. Cell Biol.* 24:188–193. https://doi.org/10.1016/j.ceb.2012.02.002

Farcomeni, A. 2008. A review of modern multiple hypothesis testing, with particular attention to the false discovery proportion. *Stat. Methods Med. Res.* 17:347–388. https://doi.org/10.1177/0962280206079046

Ferrara, N., H.P. Gerber, and J. LeCouter. 2003. The biology of VEGF and its receptors. *Nat. Med.* 9:669–676. https://doi.org/10.1038/nm0603-669

Fletcher, P.A., D.R.L. Scriven, M.N. Schulson, and E.D.W. Moore. 2010. Multi-image colocalization and its statistical significance. *Biophys. J.* 99:1996–2005. https://doi.org/10.1016/j.bpj.2010.07.006

Geiger, B., J.P. Spatz, and A.D. Bershadsky. 2009. Environmental sensing through focal adhesions. *Nat. Rev. Mol. Cell Biol.* 10:21–33. https://doi.org/10.1038/nrm2593

Gordon, E.J., D. Fukuhara, S. Weström, N. Padhan, E.O. Sjöström, L. van Meeteren, L. He, F. Orsenigo, E. Dejana, K. Bentley, et al. 2016. The endothelial adaptor molecule TSAd is required for VEGF-induced angiogenic sprouting through junctional c-Src activation. *Sci. Signal.* 9:ra72. https://doi.org/10.1126/scisignal.aad9256

Gorlewicz, A., K. Krawczyk, A.A. Szczepankiewicz, P. Trzaskoma, C. Mulle, and G.M. Wilczynski. 2020. Colocalization colormap: An ImageJ plugin for the quantification and visualization of colocalized signals. *Neuroinformatics*. 18:661–664. https://doi.org/10.1007/s12021-020-09465-9

Helmuth, J.A., G. Paul, and I.F. Sbalzarini. 2010. Beyond co-localization: Inferring spatial interactions between sub-cellular structures from microscopy images. *BMC Bioinformatics*. 11:372. https://doi.org/10.1186/1471-2105-11-372

Huang, B., M. Bates, and X. Zhuang. 2009. Super-resolution fluorescence microscopy. *Annu. Rev. Biochem.* 78:993–1016. https://doi.org/10.1146/annurev.biochem.77.061906.092014

Hummer, G., F. Fricke, and M. Heilemann. 2016. Model-independent counting of molecules in single-molecule localization microscopy. *Mol. Biol. Cell*. 27:3637–3644. https://doi.org/10.1091/mbc.E16-07-0525

Jaqaman, K., and J.A. Ditlev. 2021. Biomolecular condensates in membrane receptor signaling. *Curr. Opin. Cell Biol.* 69:48–54. https://doi.org/10.1016/j.ceb.2020.12.006

Jaqaman, K., J.A. Galbraith, M.W. Davidson, and C.G. Galbraith. 2016. Changes in single-molecule integrin dynamics linked to local cellular behavior. *Mol. Biol. Cell*. 27:1561–1569. https://doi.org/10.1091/mbc.E16-01-0018

Jaqaman, K., D. Loerke, M. Mettlen, H. Kuwata, S. Grinstein, S.L. Schmid, and G. Danuser. 2008. Robust single-particle tracking in live-cell time-lapse sequences. *Nat. Methods*. 5:695–702. https://doi.org/10.1038/nmeth.1237

Jaskolski, F., C. Mulle, and O.J. Manzoni. 2005. An automated method to quantify and visualize colocalized fluorescent signals. *J. Neurosci. Methods*. 146:42–49. https://doi.org/10.1016/j.jneumeth.2005.01.012

Kittisopikul, M., A. Vahabikashi, T. Shimi, R.D. Goldman, and K. Jaqaman. 2020. Adaptive multiorientation resolution analysis of complex filamentous network images. *Bioinformatics*. 36:5093–5103. https://doi.org/10.1093/bioinformatics/btaa627

Lachmanovich, E., D.E. Shvartsman, Y. Malka, C. Botvin, Y.I. Henis, and A.M. Weiss. 2003. Co-localization analysis of complex formation among membrane proteins by computerized fluorescence microscopy: Application to immunofluorescence co-patching studies. *J. Microsc.* 212:122–131. https://doi.org/10.1046/j.1365-2818.2003.01239.x

Lagache, T., A. Grassart, S. Dallongeville, O. Faklaris, N. Sauvonnet, A. Dufour, L. Danglot, and J.C. Olivo-Marin. 2018. Mapping molecular assemblies with fluorescence microscopy and object-based spatial statistics. *Nat. Commun.* 9:698. https://doi.org/10.1038/s41467-018-03053-x

Lagache, T., N. Sauvonnet, L. Danglot, and J.C. Olivo-Marin. 2015. Statistical analysis of molecule colocalization in bioimaging. *CytometryA*. 87:568–579. https://doi.org/10.1002/cyto.a.22629

Lampugnani, M.G., F. Orsenigo, M.C. Gagliani, C. Tacchetti, and E. Dejana. 2006. Vascular endothelial cadherin controls VEGFR-2 internalization and signaling from intracellular compartments. *J. Cell Biol.* 174:593–604. https://doi.org/10.1083/jcb.200602080

Lanahan, A.A., K. Hermans, F. Claes, J.S. Kerley-Hamilton, Z.W. Zhuang, F.J. Giordano, P. Carmeliet, and M. Simons. 2010. VEGF receptor 2 endocytic trafficking regulates arterial morphogenesis. *Dev. Cell*. 18:713–724. https://doi.org/10.1016/j.devcel.2010.02.016

Linkert, M., C.T. Rueden, C. Allan, J.M. Burel, W. Moore, A. Patterson, B. Loranger, J. Moore, C. Neves, D. MacDonald, et al. 2010. Metadata matters: Access to image data in the real world. *J. Cell Biol.* 189:777–782. https://doi.org/10.1083/jcb.201004104

Liu, A.P., F. Aguet, G. Danuser, and S.L. Schmid. 2010. Local clustering of transferrin receptors promotes clathrin-coated pit initiation. *J. Cell Biol.* 191:1381–1393. https://doi.org/10.1083/jcb.201008117

Lucas, A.M., P.V. Ryder, B. Li, B.A. Cimini, K.W. Eliceiri, and A.E. Carpenter. 2021. Open-source deep-learning software for bioimage segmentation. *Mol. Biol. Cell*. 32:823–829. https://doi.org/10.1091/mbc.E20-10-0660

Malkusch, S., U. Endesfelder, J. Mondry, M. Gelléri, P.J. Verveer, and M. Heilemann. 2012. Coordinate-based colocalization analysis of single-molecule localization microscopy data. *Histochem. Cell Biol.* 137:1–10. https://doi.org/10.1007/s00418-011-0880-5

Manders, E.M.M., F.J. Verbeek, and J.A. Aten. 1993. Measurement of co-localization of objects in dual-colour confocal images. *J. Microsc.* 169:375–382. https://doi.org/10.1111/j.1365-2818.1993.tb03313.x

Marlowe, T.A., F.L. Lenzo, S.A. Figel, A.T. Grapes, and W.G. Cance. 2016. Oncogenic receptor tyrosine kinases directly phosphorylate focal adhesion kinase (FAK) as a resistance mechanism to FAK-kinase inhibitors. *Mol. Cancer Ther.* 15:3028–3039. https://doi.org/10.1158/1535-7163.MCT-16-0366

Mascalchi, P., and F.P. Cordelieres. 2019. Which elements to build co-localization workflows? From metrology to analysis. In *Computer Optimized Microscopy: Methods and Protocols*. E. Rebollo, and M. Bosch, editors, Vol. 2040. Springer, New York. 177–213.

Mayle, K.M., A.M. Le, and D.T. Kamei. 2012. The intracellular trafficking pathway of transferrin. *Biochim. Biophys. Acta*. 1820:264–281. https://doi.org/10.1016/j.bbagen.2011.09.009

Murphy, J.M., K. Jeong, Y.A.R. Rodriguez, J.H. Kim, E.Y.E. Ahn, and S.T.S. Lim. 2019. FAK and Pyk_2 activity promote TNF-α and IL-1β-mediated pro-inflammatory gene expression and vascular inflammation. *Sci. Rep.* 9:7617. https://doi.org/10.1038/s41598-019-44098-2

Nehme, E., L.E. Weiss, T. Michaeli, and Y. Shechtman. 2018. Deep-STORM: Super-resolution single-molecule microscopy by deep learning. *Optica*. 5:458–464. https://doi.org/10.1364/optica.5.000458

Pageon, S.V., P.R. Nicovich, M. Mollazade, T. Tabarin, and K. Gaus. 2016. Clus-DoC: A combined cluster detection and colocalization analysis for single-molecule localization microscopy data. *Mol. Biol. Cell*. 27:3627–3636. https://doi.org/10.1091/mbc.E16-07-0478

Pastorek, L., M. Sobol, and P. Hozak. 2016. Colocalization coefficients evaluating the distribution of molecular targets in microscopy methods based on pointed patterns. *Histochem. Cell Biol.* 146:391–406. https://doi.org/10.1007/s00418-016-1467-y

Rigiracciolo, D.C., M.F. Santolla, R. Lappano, A. Vivacqua, F. Cirillo, G.R. Galli, M. Talia, L. Muglia, M. Pellegrino, N. Nohata, et al. 2019. Focal adhesion kinase (FAK) activation by estrogens involves GPER in triple-negative

breast cancer cells. *J. Exp. Clin. Cancer Res.* 38:58. https://doi.org/10.1186/s13046-019-1056-8

Saguy, A., T.N. Baldering, L.E. Weiss, E. Nehme, C. Karathanasis, M.S. Dietz, M. Heilemann, and Y. Shechtman. 2021. Automated analysis of fluorescence kinetics in single-molecule localization microscopy data reveals protein stoichiometry. *J. Phys. Chem. B.* 125:5716–5721. https://doi.org/10.1021/acs.jpcb.1c01130

Sahl, S.J., S.W. Hell, and S. Jakobs. 2017. Fluorescence nanoscopy in cell biology. *Nat. Rev. Mol. Cell Biol.* 18:685–701. https://doi.org/10.1038/nrm.2017.71

Simoncelli, S., J. Griffie, D.J. Williamson, J. Bibby, C. Bray, R. Zamoyska, A.P. Cope, and D.M. Owen. 2020. Multi-color molecular visualization of signaling proteins reveals how C-terminal src kinase nanoclusters regulate T cell receptor activation. *Cell Rep.* 33:108523. https://doi.org/10.1016/j.celrep.2020.108523

Simons, M., E. Gordon, and L. Claesson-Welsh. 2016. Mechanisms and regulation of endothelial VEGF receptor signalling. *Nat. Rev. Mol. Cell Biol.* 17:611–625. https://doi.org/10.1038/nrm.2016.87

Sorkin, A., and M. von Zastrow. 2009. Endocytosis and signalling: Intertwining molecular networks. *Nat. Rev. Mol. Cell Biol.* 10:609–622. https://doi.org/10.1038/nrm2748

Stauffer, W., H.J. Sheng, and H.N. Lim. 2018. EzColocalization: An ImageJ plugin for visualizing and measuring colocalization in cells and organisms. *Sci. Rep.* 8:15764. https://doi.org/10.1038/s41598-018-33592-8

Sulzmaier, F.J., C. Jean, and D.D. Schlaepfer. 2014. FAK in cancer: Mechanistic findings and clinical applications. *Nat. Rev. Cancer*. 14:598–610. https://doi.org/10.1038/nrc3792

Sun, Z., X. Li, S. Massena, S. Kutschera, N. Padhan, L. Gualandi, V. Sundvold-Gjerstad, K. Gustafsson, W.W. Choy, G. Zang, et al. 2012. VEGFR2 induces c-Src signaling and vascular permeability in vivo via the adaptor protein TSAd. *J. Exp. Med.* 209:1363–1377. https://doi.org/10.1084/jem.20111343

Sungkaworn, T., M.L. Jobin, K. Burnecki, A. Weron, M.J. Lohse, and D. Calebiro. 2017. Single-molecule imaging reveals receptor-G protein interactions at cell surface hot spots. *Nature*. 550:543–547. https://doi.org/10.1038/nature24264

Taylor, A.B., M.S. Ioannou, J. Aaron, and T.L. Chew. 2018. Model-free quantification and visualization of colocalization in fluorescence images. *Cytometry A*. 93:504–516. https://doi.org/10.1002/cyto.a.23356

Thomann, D., D.R. Rines, P.K. Sorger, and G. Danuser. 2002. Automatic fluorescent tag detection in 3D with super-resolution: Application to the analysis of chromosome movement. *J. Microsc.* 208:49–64. https://doi.org/10.1046/j.1365-2818.2002.01066.x

Valm, A.M., S. Cohen, W.R. Legant, J. Melunis, U. Hershberg, E. Wait, A.R. Cohen, M.W. Davidson, E. Betzig, and J. Lippincott-Schwartz. 2017. Applying systems-level spectral imaging and analysis to reveal the organelle interactome. *Nature*. 546:162–167. https://doi.org/10.1038/nature22369

Vicente-Manzanares, M., and A.R. Horwitz. 2011. Adhesion dynamics at a glance. *J. Cell Sci.* 124:3923–3927. https://doi.org/10.1242/jcs.095653

Wagner, A. 2000. Robustness against mutations in genetic networks of yeast. *Nat. Genet.* 24:355–361. https://doi.org/10.1038/74174

Williamson, D.J., G.L. Burn, S. Simoncelli, J. Griffié, R. Peters, D.M. Davis, and D.M. Owen. 2020. Machine learning for cluster analysis of localization microscopy data. *Nat. Commun.* 11:1493. https://doi.org/10.1038/s41467-020-15293-x

Wu, L.W., L.D. Mayo, J.D. Dunbar, K.M. Kessler, O.N. Ozes, R.S. Warren, and D.B. Donner. 2000. VRAP is an adaptor protein that binds KDR, a receptor for vascular endothelial cell growth factor. *J. Biol. Chem.* 275:6059–6062. https://doi.org/10.1074/jbc.275.9.6059

Zhang, B., J. Zerubia, and J.C. Olivo-Marin. 2007. Gaussian approximations of fluorescence microscope point-spread function models. *Appl. Optics*. 46:1819–1829. https://doi.org/10.1364/ao.46.001819

Zhang, J.Z. 2012. Genetic redundancies and their evolutionary maintenance. *Adv. Exp. Med. Bio.* 751:279–300.

Zhu, L., W. Zhang, D. Elnatan, and B. Huang. 2012. Faster STORM using compressed sensing. *Nat. Methods*. 9:721–723. https://doi.org/10.1038/nmeth.1978

Supplemental material

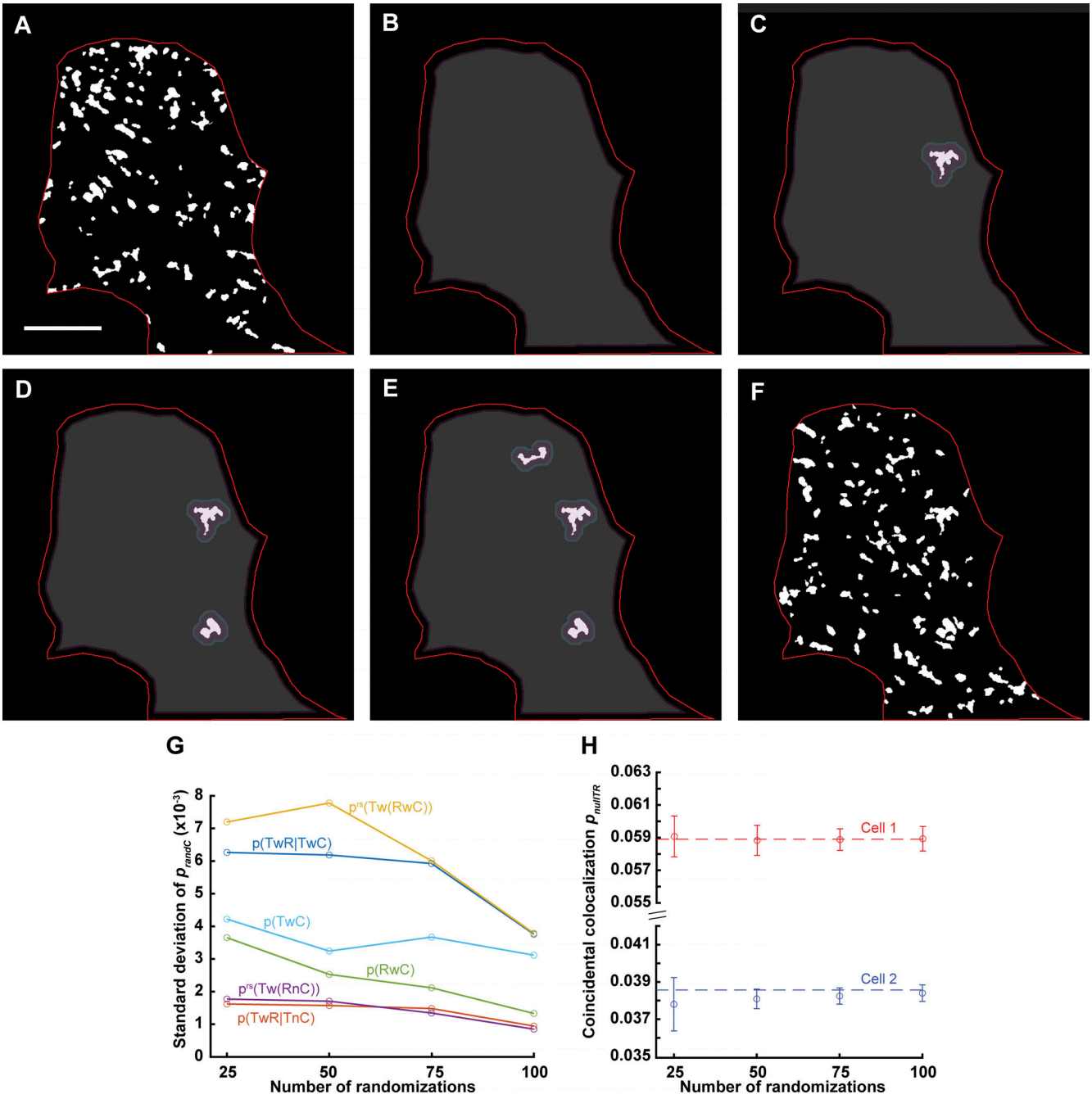

Figure S1. **Example illustrating randomization procedure for non-punctate objects and convergence of calculated coincidental measures upon randomization. (A)** Binary image of original paxillin patch segmentation. Red line outlines region of interest (ROI; the cell in the image in this case). Scale bar (applicable to all panels), 10 µm. **(B)** Available area for randomly placing the first object (gray-shaded area) within total ROI. **(C)** Random placement of first (largest) object, and the remaining available area (gray-shaded area), which excludes an area around the already placed object. **(D and E)** Random placement of second largest (D) and third largest (E) objects, and the remaining available area after each placement (gray-shaded area). **(F)** Final random placement of all objects within the ROI. **(G)** Variation of "randC" counterparts of conditional colocalization measures upon indicated number of condition object randomizations, from one representative cell. Variation is shown as the standard deviation of four repeats of the indicated number of randomizations. **(H)** Variation of $p_{nullTR}(TwR)$ upon indicated number of target object randomizations, from two representative cells. Data are shown as mean ± SD, calculated from four repeats of the indicated number of randomizations. To test the convergence of $p_{nullTR}(TwR)$, we performed this test on images with punctate target objects, for which $p_{nullTR}(TwR)$ could be also estimated using points on a grid (Fig. 2, A and B), and thus could be used as the ground truth for testing. Dashed line shows $p_{nullTR}(TwR)$ from the points on a grid calculation.

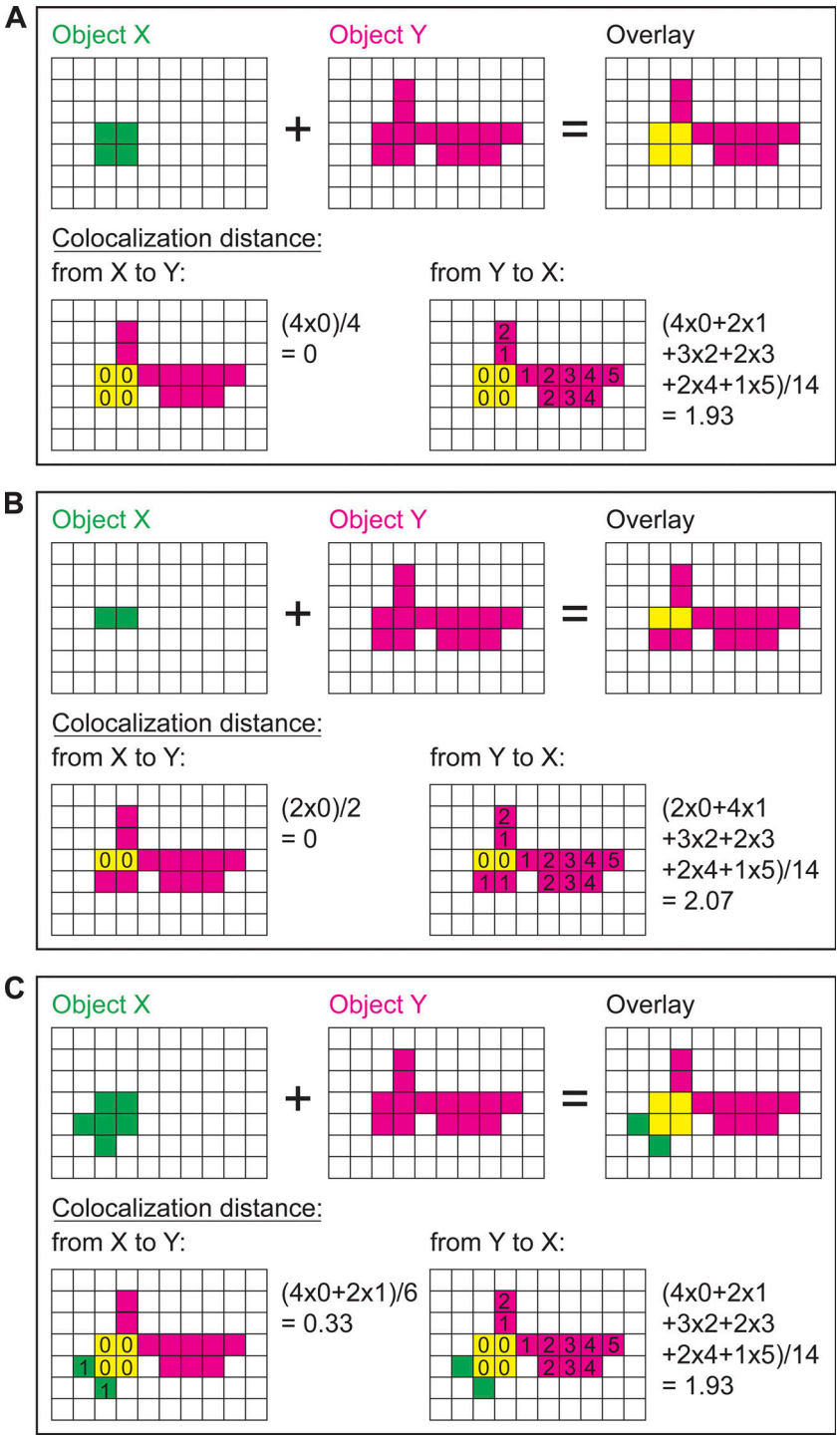

Figure S2. **Illustration of colocalization distance and its dependence on relative location, size and shape for two general, non-punctate objects.** The distance from each pixel in one object to the nearest pixel in the other object is shown on each pixel. **(A)** Object X (green) is fully colocalized with object Y (magenta), and thus the colocalization distance from X to Y is 0. Object Y, being larger than object X, is partially colocalized with object X. This is reflected in the colocalization distance from Y to X, which is 1.93. **(B)** Object X (green) is smaller in B than in A. Object X remains fully colocalized with object Y, and the colocalization distance from X to Y remains 0. However, object Y exhibits now less colocalization with object X (because X became smaller). This is reflected by the colocalization distance from Y to X, which increases from 1.93 in A to 2.07 in B. **(C)** Object X (green) is larger in C than in A. Now it is partially colocalized with object Y, and the colocalization distance from X to Y increases to 0.33. The change in object X is however immaterial for the extent of colocalization of object Y with object X, and the colocalization distance in C is the same as in A.

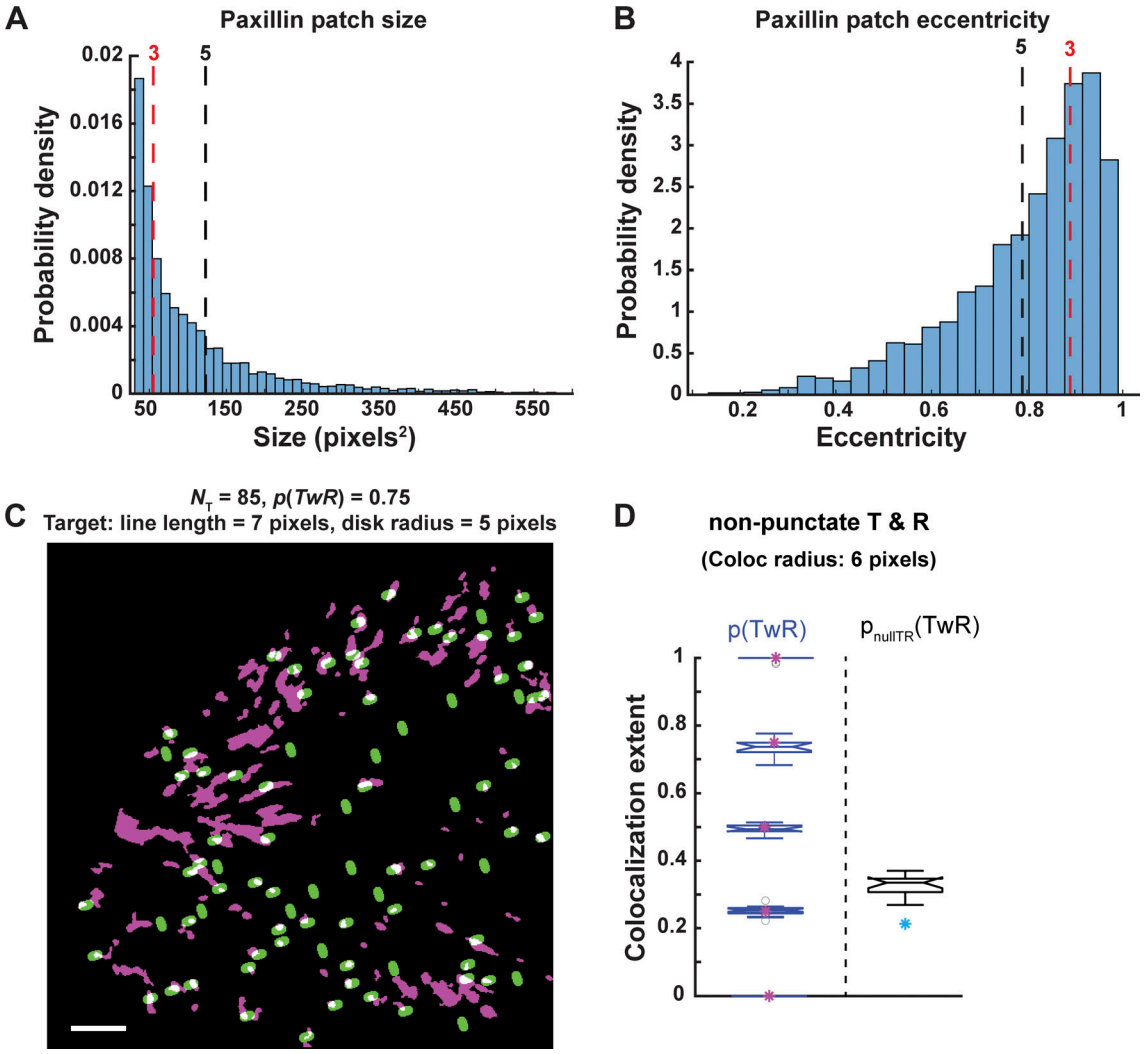

Figure S3. **Properties of segmented paxillin patches and further colocalization analysis of non-punctate objects. (A and B)** Size (A) and eccentricity (B) of segmented paxillin patches. Eccentricity values are between 0 and 1, where 0 describes a circle and 1 describes a straight line. Red and black dashed lines indicate size and eccentricity values for simulated non-punctate objects generated by dilating a line of length 7 pixels using a disk of radius 3 (red) or 5 (black) pixels. For objects using a disk of radius 3 pixels, size = 55 pixels^2 and eccentricity = 0.89. For objects using a disk of radius 5 pixels, size = 123 pixels^2 and eccentricity = 0.79. **(C)** Example simulated image with non-punctate target objects (green) and segmented paxillin patches as reference objects (magenta) with indicated simulation parameters. **(D)** Calculated $p(TwR)$ (left) and corresponding $p_{nullTR}(TwR)$ (right) for simulations of non-punctate target and reference objects, for the same data as in Fig. 2 C, but using a colocalization radius of 6 pixels. Details as in Fig. 2 C.

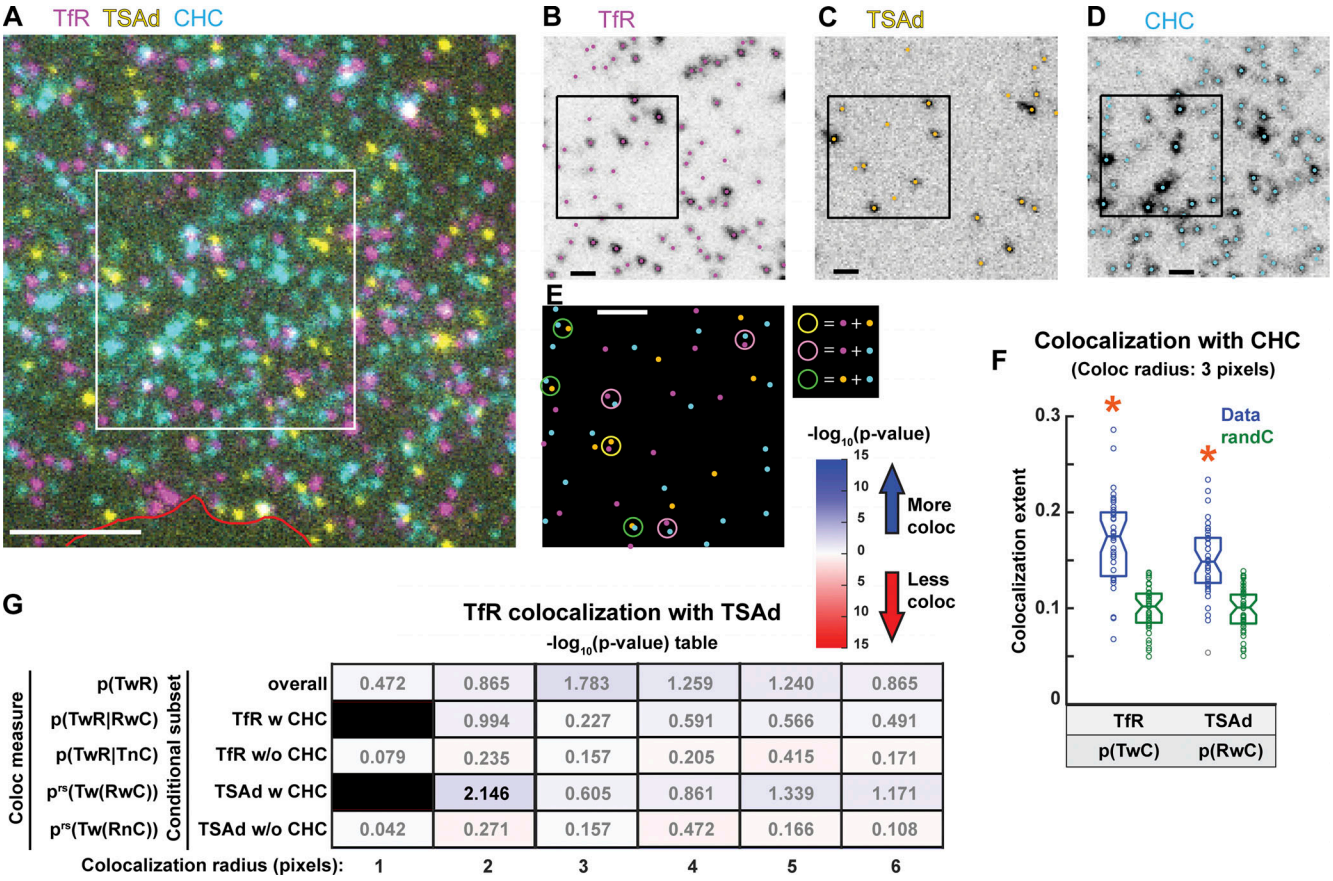

Figure S4. **Conditional colocalization analysis correctly identifies no colocalization in an experimental negative control. (A)** Representative three-color IF image of TfR, TSAd and CHC on the surface of a TIME cell imaged via TIRFM. Red line shows cell edge. Scale bar, 5 µm. **(B–D)** Particle detections (shown as dots) overlaid on the individual channels for the area within the white box in A. Scale bar, 1 µm. **(E)** Overlay of the three channel detections for the area within the black box in B–D, with color-coding following that in B–D. Colored circles (diameter = 243 nm) point out colocalization events between the different molecules, following color-coding in legend on the side. Scale bar, 1 µm. **(F)** Probabilities of target (TfR) and reference (TSAd) to colocalize with condition (CHC), together with their coincidental counterparts ("randC"). Details as in Fig. 3 F. **(G)** $-\log_{10}$(P value) table for the various conditional colocalization measures at the indicated colocalization radii. Table indicates next to each colocalization measure the molecule subset that it represents. Black-filled rectangles indicate no values due to insufficient number of datapoints for the indicated category. Other details as in Fig. 3 H. *N* = 39 cells from 4 repeats. See Table 3 for number of objects per channel and other dataset properties.

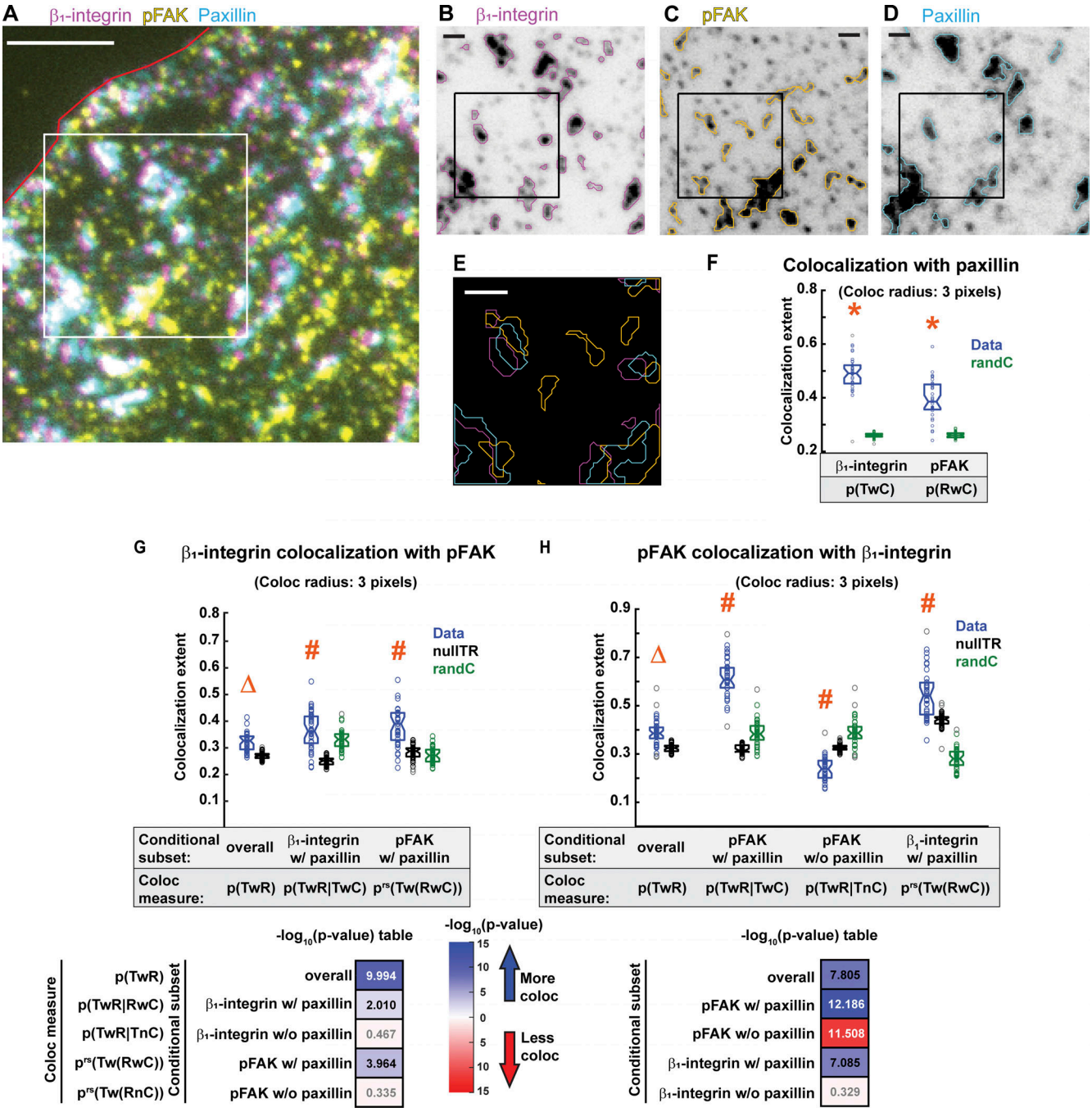

Figure S5. **Conditional colocalization analysis of non-punctate images of activated β_1-integrin, pFAK and paxillin. (A)** Representative three-color IF image of activated β_1-integrin, pFAK and paxillin on the surface of a TIME cell imaged via TIRFM. Red line shows cell edge. Scale bar, 5 µm. **(B–D)** Patch segmentation (shown as outlines) overlaid on the individual channels for the area within the white box in A. Scale bar, 1 µm. **(E)** Overlay of the three channel segmentations for the area within the black box in B–D, with color coding following that in B–D. Scale bar, 1 µm. **(F)** Probabilities of β_1-integrin and pFAK to colocalize with the condition (paxillin; representing FAs), together with their coincidental counterparts ("randC"), using the indicated colocalization radius. Details as in Fig. 3 F. **(G and H)** Conditional colocalization measures and their coincidental counterparts ("nullTR" and "randC") (top) and $-\log_{10}$(P value) table summarizing the significance of each conditional colocalization measure (bottom), at the indicated colocalization radius for target = β_1-integrin, reference = pFAK (G) and vice versa (H), both with condition = paxillin. Only significant conditional colocalization measures, together with *p(TwR)*, are shown in boxplot form. Boxplot figure details as in Figs. 3 G and 6 G. $-\log_{10}$(*P* value) table details as in Fig. 3 H. The molecule subsets listed to the left of the tables correspond to the colocalization measures on the far left of G. In F–H, randC and nullTR were calculated using 50 randomizations instead of 100 for computational efficiency. Similar to the analysis shown in Fig. 3, this analysis using all non-punctate objects also revealed that paxillin promotes β_1-integrin-pFAK colocalization. The colocalization measures have overall higher values here, with some gaining significance relative to Fig. 3, probably because of the more complete observation of β_1-integrin and pFAK here, prior to their photobleaching to obtain punctate signals (as used for analysis shown in Fig. 3). *N* = 37 cells from four repeats. See Table 4 for number of objects per channel and other dataset properties.